



Alexandria University
Alexandria Engineering Journal

www.elsevier.com/locate/aej
www.sciencedirect.com



3D RT adaptive path sensing Method: RSSI modelling validation at 4.5 GHz, 28 GHz, and 38 GHz



Tan Kim Geok^a, Ferdous Hossain^b, Sharul Kamal Abdul Rahim^c,
Olakunle Elijah^{d,*}, Akaa A. Eteng^e, Chun Theng Loh^f, Lim Li Li^g, C.P. Tso^h,
Tharek Abd Rahmanⁱ, M. Nour Hindia^j

^a Faculty of Engineering and Technology, Multimedia University, Melaka 75450, Malaysia

^b Faculty of Engineering and Technology, Multimedia University, Melaka 75450, Malaysia

^c Wireless Communication Centre, Faculty of Electrical Engineering, Universiti Teknologi Malaysia, 81310 Skudai, Johor, Malaysia

^d Wireless Communication Centre, Faculty of Electrical Engineering, Universiti Teknologi Malaysia, 81310 Skudai, Johor, Malaysia

^e Department of Electrical/Electronic Engineering at the University of Port Harcourt, Nigeria

^f Faculty of Engineering and Technology, Multimedia University, Melaka 75450, Malaysia

^g Faculty of Engineering and Technology Tunku Abdul Rahman College (TARC), Kuala Lumpur, Malaysia

^h Faculty of Engineering and Technology, Multimedia University, Melaka 75450, Malaysia

ⁱ T. A. Rahman is with the Faculty of Electrical Engineering, Universiti Teknologi Malaysia, 81310 Skudai, Johor, Malaysia

^j Faculty of Engineering, Department of Electrical Engineering, University of Malaya, 50603 Kuala Lumpur, Malaysia

Received 9 December 2021; revised 1 April 2022; accepted 18 April 2022

KEYWORDS

Measurement;
Modelling;
Radio propagation;
Ray tracing;
RSSI

Abstract This paper explains a new Adaptive Path Sensing Method (APSM) for indoor radio wave propagation prediction. Measurement campaigns, which cover indoor line-of-sight (LoS), non-line-of-sight (NLoS) and different room scenarios, are conducted at the new Wireless Communication Centre (WCC) block P15a of Universiti Teknologi Malaysia (UTM), Johor, Malaysia. The proposed APSM is evaluated through a computerized modelling tool by comparing the Received Signal Strength Indicator (RSSI) with measurement data and the conventional Shooting-Bouncing Ray Tracing (SBRT) method. Simulations of the APSM and SBRT are performed with the same layout of the new WCC block P15a by using the exact building dimensions. The results demonstrate that the proposed method achieves a better agreement with measured data, compared to the conventional SBRT outputs. The reduced computational time and resources

* Corresponding author at: Wireless Communication Centre, Faculty of Electrical Engineering, Universiti Teknologi Malaysia, 81310 Skudai, Johor, Malaysia.

E-mail addresses: kgtan@mmu.edu.my (T. Kim Geok), ferdous.mbstu.cse@gmail.com (F. Hossain), sharulkamal@fke.utm.my (S. Kamal Abdul Rahim), elij_olak@yahoo.com (O. Elijah), akaa.eteng@gmail.com (A.A. Eteng), 1151105480@student.mmu.edu.my (C. Theng Loh), llim@tarc.edu.my (L. Li Li), cptso@mmu.edu.my (C.P. Tso), tharek@utm.my (T. Abd Rahman), nourhindia@hotmail.com (M. Nour Hindia).

Peer review under responsibility of Faculty of Engineering, Alexandria University.

<https://doi.org/10.1016/j.aej.2022.04.033>

1110-0168 © 2022 THE AUTHORS. Published by Elsevier BV on behalf of Faculty of Engineering, Alexandria University
This is an open access article under the CC BY-NC-ND license (<http://creativecommons.org/licenses/by-nc-nd/4.0/>).

required are also important milestones to ray tracing technology. The proposed APSM method can assist engineers and researchers to reduce the time required in modelling and optimizing reliable radio propagation in an indoor environment.

© 2022 THE AUTHORS. Published by Elsevier BV on behalf of Faculty of Engineering, Alexandria University This is an open access article under the CC BY-NC-ND license (<http://creativecommons.org/licenses/by-nc-nd/4.0/>).

1. Introduction

Ray tracing is implemented in radio wave propagation prediction models, where it detects all the possible paths of the ray depicting a transmission [1]. It identifies the path based on a single point in front of the radiated wave. Ray tracing applies the concept of light in the reverse way, whereby the path generated is traced back from the receiver to the source [2].

Generally, the ray tracing process can be divided into 3 major steps. Firstly, ray tracing depicts the ray at every angle and simulates the ray path in a certain layout, either indoor or outdoor propagation, complying with Geometric Optics (GO) [3,4] and the Uniform Theory of Diffraction (UTD) [5,6]. Then, ray intersection occurs, where several light phenomena such as reflection [7], refraction [8], diffraction [9], and scattering [10] take place depending on the environment layout [11,12]. Lastly, all the rays are gathered and propagated to the receiving site. These rays are usually collected to analyse and evaluate the behaviour of the propagation. For example, RSSI at the receiver can be used to estimate the power level from router to client point after deducting possible antenna and cable loss [13,14]. A larger value of RSSI indicates a stronger signal [15].

With regards to the ray-tracing technique [16], there are a few existing methods available [17] to model radio wave propagation. For example, the imaging technique is well-known and widely used to detect the path of rays from transmitter to receiver, due to its simplicity and efficiency [18]. Image technique is suitable and reliable to identify the ray path involving several reflections; however, it possesses the disadvantages of the large number of reflection objects required and the long computational time.

An example of the use of ray tracing is found in [19], where a wave propagation prediction model using image theory is proposed. The shift of rays obstructing the obstacle is taken into consideration to create a more accurate computation. Zamani et al. [20] used the image method to estimate the boundary at a high accuracy level. Valenzuela et al. [21] has proven that increasing the number of reflections results in lower prediction error while increasing the overall computational time exponentially.

The Shooting and Bouncing Ray Tracing (SBRT) method act as the fundamental principle to analyse and predict the signal [22]. This method was first introduced by Ling et al. [23], whereby multiple reflections are considered. In the SBRT method, the transmitter generates rays after detecting they have reached the receiver or an obstacle. During this period, phenomena such as diffusion, refraction, or scattering of rays may occur along with the characteristics of the ray. Then, the field energy is measured concerning the associated ray after the ray has been received by the receiver. Teh et al. [24] had come

out with an SBRT improvement ray tracing algorithm for radio propagation modelling. Yun et al. [25] presented an SBRT extraction algorithm that improves computational time at fixed memory resources. Dama et al. [26] developed a dual-band MIMO system operating at 2.4 GHz and 5 GHz in a typical office building. It achieved the agreement between the predicted result and the measured result through the SBRT method. The computational efficiency could also be enhanced using the SBRT method in a GPU-based system. This was shown in [27] where the result showed a 16 times improvement compared to the conventional CPU.

In a complex environment with several receivers positioned, conventional models, express their high complexity. The receiver zone is not defined in these conventional methods. These require huge numbers of rays to be propagated from the base station to the surrounding by using a predefine vertical and horizontal angle. The high-resolution rays are blindly launched, where they are either encountered with receiver capture sphere or lost energy and disappeared. In this case, the complexity arises as the tracing process for each ray is extremely complex, resulting in a huge amount of resources and computational time.

In this paper, a 3-D ray-tracing APSM is presented and implemented in a computerized in-house simulator, along with the conventional SBRT methods which were verified by measurement. The simulation is executed based on the actual building measurement layout at WCC block P15a, located at UTM, Johor, Malaysia. The simulation result is then compared with the experimental result performed at the same location. Hence, the contributions of this paper are highlighted as follows:

- A new ray launching method called APSM is developed and a new simulator is developed for the study of APSM approach for indoor radio propagation that takes into account the attenuation from the ceiling and floor in addition to the effect of walls.
- In the proposed APSM, the number of ray launching is greatly reduced, the computational complexity and time is also reduced when compared with the renowned SBRT method. The results have been verified with respect to measurement data in an indoor study environment.

The paper is organized in the following way: Section II discusses the related works while Section III introduces the mathematical equations for radio wave propagation modelling. Section IV presents the concept of the proposed adaptive path sensing method, section V discusses the measurement environment and experimental procedures, and section VI reports and discussed the experimental results. Finally, in section VII, a conclusion and envisioned future development is drawn.

2. Related work

There have been several works on indoor propagation measurement. For example, Beauvarlet and Virga [28] have investigated the fading characteristic of small-scale indoor propagation using directional antennas. The path loss was obtained in the experimental setup and compared to Rician and Nakagami distribution models. However, the experiment was limited to the 30 GHz range, where the scope is narrowed down to the millimeter-wave (mmW) band. Meanwhile, Wang et al. [29] had achieved high accuracy and reliability on radio propagation characteristics prediction for the indoor environment. However, the algorithm was not subjected to experimental validation, and only simulation results were obtained. In [30], measurement campaigns at indoor environments such as offices and classrooms were held for mmW propagation at 28 GHz. Propagation parameters such as delay and angles were estimated through the proposed algorithm. A propagation measurement and modelling at ultra-wideband was presented by Briso et al. [37] in a large indoor environment exposed to the usage of the wideband in sensors application. Cheffena [31] proposed a simulated technique for industrial indoor measurement with proven consistency as the Saleh-Valenzuela model. The advantage of this technique was the simulation of large scenarios by considering the size, type, and orientation of material [32]. However, it possessed the same problem as the previous work, without validation of the developed indoor multipath model using an appropriate real-life setup. Jong et al. [33] had performed a two-directional propagation in indoor office environments, covering the frequency bands from 2.4 to 61 GHz.

Other examples include a 28 GHz radio channel measurement, reported in [47]. A similar measurement setup with a 26 dBi horn antenna was conducted by Lei et al. [48] to investigate the propagation characteristics in terms of path loss, root mean square delay spread, and power angular profiles in an indoor scenario. Also, Sun et al. [57] and Deng et al. [49] had conducted an indoor office measurement campaign at 28 GHz and 73 GHz. The measurement results were analysed and validated with different path loss models, which were more accurate than the 3rd Generation Partnership Project (3GPP) and International Telecommunication Union (ITU) indoor propagation model that requires a high number of parameters and has a less physical basis. Using a similar frequency setting, Deng et al. [50] presented a mmW measurement in an office environment. The findings demonstrated an effective channel model for mm-wave signal simulation and communication system development. Similarly, a measurement campaign for an indoor corridor and office was presented in [34] for 8 GHz to 11 GHz. In [35] an indoor MIMO measurement for NLOS condition at 2.55 GHz and 24 GHz was carried out. The ray tracing simulation presented by Mani and Oestges [36] included the feature of penetration to enhance prediction accuracy. The outputs of the simulation such as cross-polarization level and delay spread were obtained and compared with the measurement, but the prediction alignment with the experimental result still required improvement. Hence, in this paper, a more comprehensive indoor wave propagation modelling is proposed.

There are also recent simulator developments for ray tracing techniques in radio wave propagation prediction, such as

in [37]. For example, Yoon et al. [38] had proposed an intelligent ray tracing method, which accelerated the simulation time. This algorithm reused the ray path construction of the first ray onto the other rays, which effectively eliminated the unnecessary prediction process for the other rays. The simulation was held in a simple room, which was 13.0 m in length, 8.6 m in width, and 2.7 m in height, where only 5 reflections were considered. Zhou and Jacksha [39] had presented a ray-tracing method to model the radio frequency in the tunnel environment. Azpilicueta et al. [40] had introduced the convergence method in indoor environment wave estimation. This method involved obtaining the parameters such as the number of reflections and launching rays first before implementing them into the simulation. For example, 6 reflections and 64,800 launching rays were incorporated into the simulation for iRadio Laboratory located at the University of Calgary. The 3-D ray launching algorithm proposed by Granda et al. [46] was one of the remarkable achievements in 3-D ray tracing. The angular resolution of $\pi/180$ rad was used to model an urban scenario dimension at 868 MHz, 2.4 GHz, and 5.9 GHz. The result showed a notable accuracy compared with the conventional 2-D analytical path loss model.

However, in a high complexity environment with multiple receivers positioned, these models possess their disadvantages. In these conventional methods, the receiver zone is not defined. They require large numbers of rays to be propagated from the base station to the surrounding by using a predefine vertical angle (θ) and horizontal angle (Φ), as mentioned in [41]. In other words, more rays are needed to cover the propagation area since the zone of propagation is not pre-defined. The high-resolution rays are blindly launched, where they are either encountered with receiver capture sphere or lost energy and disappeared. Consequently, the weakness arises as the tracing process for each ray is extremely complex, resulting in a huge amount of resources [42–43] and computational time [44]. These problems have a notable impact on area coverage, propagation distance, as well as path loss [45]. This is proven in [46], where the conventional ray-tracing method had reduced accuracy and many complex calculations through Finite Difference Time Domain (FDTD) analysis.

Simulations have also been recently performed at 4.5 GHz, 28 GHz and 38 GHz. For example, in [51], a smart ray tracing method was proposed in the simulation for indoor radio propagation prediction at 28 GHz. In [52], Hossain et al. had introduced the method for indoor wave propagation at 4.5 GHz. The output of the simulation was emphasized more on path loss and received signal strength indication level. Geok et al. [53] had come out with a general ray tracing technique to minimize the number of launching rays known as Minimum Ray Launching Maximum Accuracy (MRLMA). This technique was applicable for the indoor environment as it was advantageous in terms of coverage and simulation time. A similar setup was also used in [63–64], where mm-wave application at 28 GHz and 38 GHz was done for indoor propagation prediction. However, the main limitation was the non-consideration of ceiling effects. In [54], a comprehensive review of the hybrid approach was presented along with its effectiveness in reducing computational time. Similarly, in [55], a new ray tracing method was proposed and verified in a simple room through simulation. The methods above considered the wall as the only obstacle [56].

In summary, some of the limitations identified from the related works include lack of experimental validation, use of conventional ray-tracing SBRT methods with high computational complexity, non-realistic indoor scenarios by considering only the attenuation from the ceiling in the indoor environment. To address these issues, in this research, a 3-D ray-tracing APSM method is proposed to overcome the challenge of time and computational complexity related to the conventional SBRT method. Furthermore, the APSM method is validated by comparing the performance with the SBRT and measurement campaign using RSSI in a more realistic building layout that accounts for ceiling and floor attenuation.

3. Radio propagation modeling equations

Rays have the same concept as light which propagates in a straight line. Friis transmission equation [57] is the fundamental equation to calculate the power received in radio propagation, as in Eq. (1).

$$\frac{P_r}{P_t} = G_t G_r \left(\frac{\lambda}{4\pi r} \right)^2 \quad (1)$$

The symbols P_r and P_t indicate receiver power and transmitter power, while G_t , G_r , λ and r represent transmitter antenna gain, receiver antenna gain, wavelength, and the separation distance between two antennae, respectively.

Maxwell equations [58] can also be used in predicting radio propagation. For example, the electric field can be expressed as shown in Eq. (2).

$$\bar{E}(r) = \bar{e}(r) e^{-j\beta_0 S(r)} \quad (2)$$

In Eq. (2), β_0 approaches infinity for high frequency. The term $\bar{e}(r)$ indicates the magnitude vector while $S(r)$ indicates eikonal or travel path. The assumption in this paper is that the rays are mainly propagating in straight lines while maintaining in the same medium as that before hitting an obstacle.

The derivations of the Fresnel equation are shown below. Eq. (3) and Eq. (4) show the equation for boundary conditions for E-field and H-field respectively.

$$E_i + E_r = E_t \quad (3)$$

$$B_i \cos\theta_i - B_r \cos\theta_r = B_t \cos\theta_t \quad (4)$$

By using the law of reflection and relationship between B and E , Eq. (4) can be written as

$$\frac{n_i E_i}{c_o} \cos\theta_i - \frac{n_i E_r}{c_o} \cos\theta_r = \frac{n_t E_t}{c_o} \cos\theta_t \quad (5)$$

Some mathematical derivations from Eq. (5) yield

$$(n_i \cos\theta_i)(E_i - E_r) = n_t E_t \cos\theta_t \quad (6)$$

By substituting Eq. (3) into Eq. (6), we obtain

$$(n_i \cos\theta_i)(E_i - E_r) = n_t (E_i + E_r) \cos\theta_t \quad (7)$$

The relationship between impedance Z with E and n is shown in Eq. (8).

$$Z = \frac{E}{H} = \frac{c_o \mu}{n} \quad (8)$$

The transmission and reflection coefficients between two homogenous media are specified in Fresnel Eqs. (9) and (10) [59]. This is applied in radio wave propagation since in an indoor environment the obstacles are electrically larger than one wavelength.

$$\Gamma_s = \frac{Z_2 \cos\theta_i - Z_1 \cos\theta_r}{Z_2 \cos\theta_i + Z_1 \cos\theta_r} \quad (9)$$

$$\Gamma_p = \frac{Z_2 \cos\theta_r - Z_1 \cos\theta_i}{Z_2 \cos\theta_r + Z_1 \cos\theta_i} \quad (10)$$

The symbols Γ_s and Γ_p represent vertical and horizontal polarizations reflection coefficients, respectively. The impedance of the medium is represented by Z_1 and Z_2 , while the angle of incidence and reflection are symbolized by θ_i and θ_r accordingly.

Diffraction occurs when a ray produces a cone of rays after reflecting at a sharp edge or object [60]. In this case, the knife-edge method is applied in the simulation to handle diffracted rays as the calculation of diffracted ray is more complicated than a simply reflected ray. In normal cases, the power level of the diffracted ray is much lower as compared to the ray in LoS [61]. The diffracting point generates its subordinate sources, causing increasing difficulty in implementing diffraction into the ray tracing algorithm. This can be solved by using the Geometrical Theory of Diffraction (GTD), where the point power level E_{GTD} is calculated in Eq. (11).

$$E_{GTD} = E_o \frac{e^{-jkp'}}{p'} D_{\parallel}^{\pm} \sqrt{\frac{p'}{p(p'+p)}} e^{-jkp} \quad (11)$$

Here, the symbol E_o represents the source point amplitude, k is the wave number, p is the distance between transmitter and receiver, p' is the diffraction point to reflection point, and D_{\parallel}^{\pm} is the diffraction coefficient. In non-conducting obstacle cases, D_{\parallel}^{\pm} can be calculated with Eq. (12).

$$D_{\parallel}^{\pm} = \frac{-e^{-j(k(p+p')+\frac{\pi}{4})}}{2n\sqrt{2\pi k} \sin\beta} \left\{ \frac{F(kLa^+(\phi-\phi'))}{\tan\left[\frac{\pi+\phi-\phi'}{2n}\right]} + \frac{F(kLa^-(\phi-\phi'))}{\tan\left[\frac{\pi+\phi-\phi'}{2n}\right]} + \Gamma_0_{\parallel}^{\pm} \frac{F(kLa^-(\phi-\phi'))}{\tan\left[\frac{\pi+\phi-\phi'}{2n}\right]} + \Gamma_n_{\parallel}^{\pm} \frac{F(kLa^+(\phi-\phi'))}{\tan\left[\frac{\pi+\phi-\phi'}{2n}\right]} \right\} \quad (12)$$

The symbols $\Gamma_0_{\parallel}^{\pm}$ and $\Gamma_n_{\parallel}^{\pm}$ represent horizontal and vertical polarization reflection coefficients, respectively. Symbol ϕ expresses forward directions while ϕ' indicates the reverse phase. The other simplified terms include $L = (pp'(p+p'))$, $\beta = \phi + \phi'$. In the simulator, a single ray with a maximum of 25 interactions is incorporated into the calculations.

In an indoor environment [62], the relationship among the received electric field of receiving ray E_R , transmitted field strength E_o , transmitter and receiver field radiation pattern $f_{Ti} f_{Ri}$ reflection coefficient for the j^{th} reflector R_j , the transmission coefficient of wall T_k , diffraction coefficient D_i , spatial

attenuation coefficient A_t and phase factor e^{-ikd} corresponding to distance d is shown in Eq. (13).

$$E_R = E_{OfT_i} f_{R_i} \left\{ \prod_j R_j \prod_k T_k \prod_t A_t D_t \right\} \frac{e^{-ikd}}{d} \quad (13)$$

The receiver power's large scale (LS) effect of the broadcast network can be easily described by path loss (PL). PL can be used to calculate the LS fading activities relying on receiver signal attenuation as a function of distance and frequency. Eq. (14) can be used to calculate the PL for LoS and NLoS scenarios.

$$PL(f, d)[dB] = FSPL(f, 1m) + 10n \log_{10} \frac{d}{1[m]} + X_\sigma \quad (14)$$

Path loss exponent is symbolized by n while X_σ denotes zero-mean Gaussian arbitrary variable concerning the standard deviation σ . FSPL with a distance of 1 m in free space can be calculated by Eq. (15), where f and c denote the operating frequency and speed of light, respectively.

$$FSPL(f, 1m)[dB] = 20n \log_{10} \frac{4\pi f}{c} \quad (15)$$

Vertical to the omnidirectional polarized environment [63], the path loss of LoS scenario and NLoS scenario are simplified to Eq. (16).

$$PL_{LOS}(d_i) = \sqrt{\sum_{i=1}^{i=i+1} \left\{ |PL_{V-Omni} - PL_{V-V}|^2 \right\}} \quad (16)$$

The total RSSI after considering Eqs. (13) and (15) can be expressed in terms of electric field and voltage as in Eq. (17).

$$\begin{aligned} P_r &= \frac{|\sum_{n=0}^M V_{rn}|^2}{R_O} = \frac{\lambda^2}{4\pi n_O} \left| \sum_{n=0}^M (E_n \bar{a}_{rn}) \sqrt{G_{rn}} \right|^2 \\ &= T = t \times \left[\left(\frac{\theta_H}{\Delta\varphi} \times \frac{\theta_V}{\Delta\theta} \right) + 4n \right] T \\ &= t \times \left[\left(\frac{\theta_H}{\Delta\varphi} \times \frac{\theta_V}{\Delta\theta} \right) + 4n \right] \frac{\lambda^2}{4\pi n_O} \\ &\times \left| \sum_{n=0}^M \left(\frac{E_O e^{-jk s_n} \sqrt{G_{rn} G'_{rn}}}{P_n} \tilde{a}_{rn} \left(\prod_{i=0}^{a_n} R_{in} A_{rin} \right) \hat{A} \cdot \right. \right. \\ &\left. \left. \times \sum_{j=0}^{b_n} \left(\prod_{j=0}^{b_n} T_{jn} A_{tjn} \right) \left(\prod_{m=0}^{c_n} D_{nm} A_{dmn} \right) \tilde{a}_{rn} \right| \right|^2 \end{aligned} \quad (17)$$

The actual measured voltage V_{rn} depends on the types of receiving antenna and types of polarization. V_{rn} can be calculated from Eq. (18).

$$V_{rn} = \sqrt{\frac{\lambda^2 G_{rn} R_O}{4\pi}} (E_n \tilde{a}_{rn}) e^{j\phi} \quad (18)$$

The symbols from Eq. (17) and Eq. (18) include: λ represents the wavelength; R_O is the receiver characteristic impedance, G_{rn} expresses the receiver directivity from which the ray arrives; \tilde{a}_{rn} is the receiving antenna polarization from which the ray arrives; $e^{j\phi}$ is the phase shift introduced by the receiving antenna. M from Eq. (17) indicates the total number of valid paths.

4. Ray tracing method

A. SBRT Method

In the conventional ray-tracing method, each ray emitted in all directions is to be performed a calculation to determine

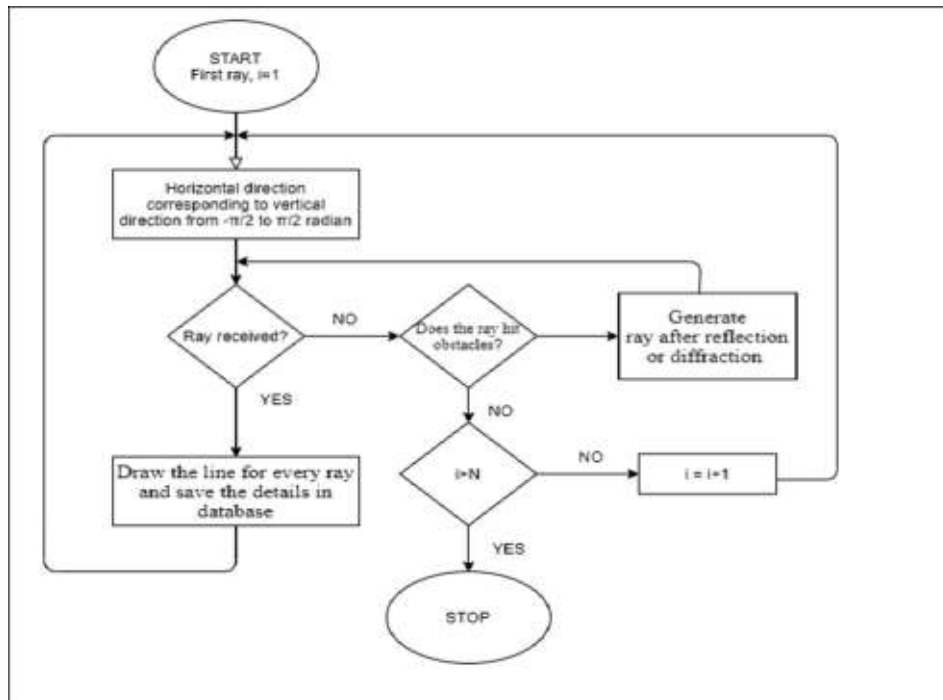


Fig. 1 Flowchart of SBRT.

whether it reaches the preset receiving zone, or disappears from the ray-tracing simulation when it is not intercepted by the receiving sphere. As a result, the method consumes long computational time and large resources, as numerous rays are to be traced in the simulation. A flowchart of the SBRT method is illustrated in Fig. 1.

B. APSM Method

In APSM, the algorithm is focused on launching the rays to the specific receiving zone, rather than emitting the rays in all directions. Each of the rays may encounter light phenomena such as reflection and diffraction and responds differently.

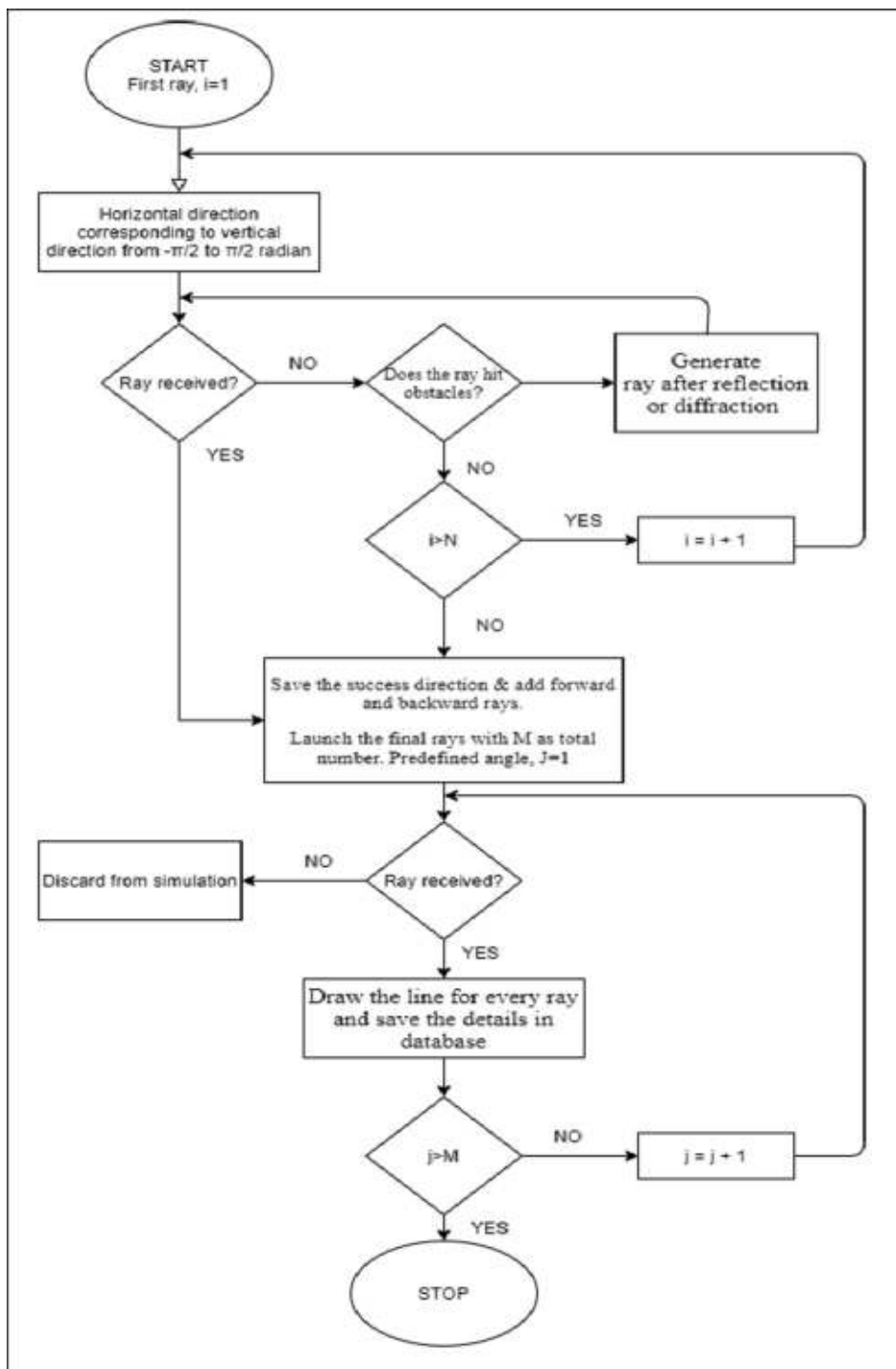


Fig. 2 Flowchart of APSM.

The proposed method identifies mathematically the relevant ray paths from the target point back to their emitting sources. The horizontal angle is measured from a horizontal reference direction, while the vertical angle is the azimuthal angle measured from a vertical direction. The APSM is illustrated in Fig. 2.

The first step in APSM is to create the building layout in the simulation environment, including all the necessary obstacles such as the wall, ceiling, and floor, as well as the Tx and Rx in the simulation. The actual geometry will be used to model the building layout.

In Step II, the propagation of rays will be traced to the receiver. The rays may undergo reflection, refraction, and diffraction before reaching the receiver. The rays are launched at regular vertical angle steps of $(\pi/180)$ radian for each of the horizontal angles. For the case of horizontal angle steps, a lower resolution is used, which is $(\pi/60)$ radian instead of $(\pi/180)$ radian. This is because the vertical step size only has little effect on the simulation result, where in this method the computational time is reduced to 3 times shorter since there are more rays to be calculated in the conventional method.

In Step III, pre-ray tracing is performed based on the calculation to identify the successive rays which are reaching the receiver zone. Next, the forward direction rays are added to each of the successive rays, where the steps size is either $\pi/180$, $\pi/240$, $\pi/360$, or $\pi/720$, based on the simulation scenario. The example of code in C# is shown below. The same goes for Step V; certain backward direction rays are added to every successive vertical angle. The steps size can be $-\pi/180$, $-\pi/240$, $-\pi/360$ or $-\pi/720$, based on the simulation scenario. In Step VI, the combination of all the probable angles from Step IV and V will be carried out. The resultant angle is more precise concerning the receiving zone. Finally, in Step VII, the launching of rays occurs, where all the emitted rays are traced and represented in colour; blue for LoS and red for NLoS. The simulation result is then saved in the database for further analysis.

5. Experimental measurement and simulation details

This section will be separated into 2 sub-sections. Section A is on the real-world measurement campaign and Section B is on the in-house simulation.

A. Measurement Environment and Experimental Setup

A measurement campaign is conducted on the ground floor of the new WCC block P15a located at UTM, Johor, Malaysia. It is a 2-storied-structure with external walls, and internally there are rooms and laboratories separated by internal walls. The carrier frequencies of 4.5 GHz, 28 GHz, and 38 GHz are used to model the indoor radio wave propagation that could potentially be used as mobile communication network bands.

A directional horn antenna is used as the base station to transmit the signal. The Tx height is set to be 2 m from the ground level, and it is connected to an MG369xC model signal generator to synthesize the waves of continuous radio signals, as antenna height has a huge impact on the coverage [64,65]. Tx horn antenna is vertically polarized and the beamwidth is 18 degrees.

On the receiver side, an omnidirectional antenna acts as the mobile station to receive the signal. It is connected to an MS2720T model spectrum analyzer where its channel bandwidth is fixed at 100 kHz. The height of Rx [66] is set to be 1.5 m. In this experiment, Rx is mainly used to measure and quantify the received power level in terms of RSSI. The hardware configuration is as shown in Table 1.

The experiment is conducted with one Tx and 83 Rx. The location of Tx is fixed at the corridor outside the prototype laboratory 1 (Room 2), as shown in Fig. 3, while 83 Rx are scattered over the 21 m \times 30 m ground floor to provide good coverage for analysis. Among these 83 sites, site 1 to 14 are used to represent the LoS scenario, and site 17 to 33 are used to model NLoS cases. The measurement is held by placing the Rx at site 1, over a distance of 1 m from Tx. The received signal from that particular location is then recorded in terms of RSSI. Then, Rx is repositioned at site 2 to carry out the measurement. This process is repeated until all 83 sites are assessed for 4.5 GHz, 28 GHz, and 38 GHz, respectively.

B. In-house Simulation

The SBRT and APSM are implemented in the in-house simulator to compare with the experimental measurements.

Table 1 MEASUREMENT PARAMETERS.

Parameter	Values		
Frequency	4.5 GHz	28 GHz	38 GHz
Height of Tx horn antenna	2 m		
Height of Rx omnidirectional antenna	1.5 m		
Transmit power	25 dBm		
TX horn antenna gain	10 dBi	19.2 dBi	21.1 dBi
RX Omni Antenna Gain	3 dBi		



Fig. 3 Experimental setup at WCC block P15a [63]

Table 2 SIMULATION CONFIGURATION.

Parameter	Values		
Frequency (GHz)	4.5	28	38
Number of pixels per meter	40		
Maximum number of interactions	25		
Resolution (degree)	1		
Tx antenna gain (dBi)	10	19.2	21.1
Rx antenna gain (dBi)	3		
Cable Loss (dB)	14.1	13.9	14.25
Floor Height (meter)	2		

through equations and stored in the database for analysis, where the RSSI of measurement campaign, SBRT, and APSM method are compared and contrasted. The simulation parameters and configuration are shown in Table 2, similar to the parameters in the measurement campaign (refer to section V-A).

6. Results and discussions

A. Results for 4.5 GHz

Fig. 5 (a) and Fig. 5 (b) show the 2-D and 3-D layouts of SBRT method simulations at 4.5 GHz, respectively. Similarly, 2-D and 3-D layouts for the APSM simulation at 4.5 GHz are shown in Fig. 4 (c) and (d), respectively.

Fig. 6 shows the RSSI data obtained from the measurement campaign (section IV-A), SBRT method, and APSM method implemented in the simulation (section IV-B) at 4.5 GHz for the LoS and NLoS scenarios and presented in Table 3 for all scenarios. The mean RSSI from measurement is -59.54 dBm. The conventional SBRT method has the mean RSSI of -67.25 dBm with an average RSSI difference of -7.71 dBm compared to measurement data. On the other hand, our proposed APSM method has the mean RSSI of -60.85 dBm with

an average RSSI difference of -1.31 dBm compared to measurement data. The percentage of error of APSM is 2.2 %, whereas the SBRT method has a percentage of error of 12.95 %. This shows that APSM has a higher agreement with measurement results in terms of RSSI power level. SBRT method has launched a total of 64,800 rays in the simulation. This is effectively reduced to 25,741 rays in APSM, with an approximate 60.28% reduction in the computational resource which can achieve higher accuracy. The same goes for the time taken to launch the ray, where the SBRT method uses 23317.44 ms to launch while APSM uses only 7620.55 ms for the whole simulation. APSM reduces the time taken for the launching ray by 67.32 %. Receivers 1 to 16 are considered as in LoS condition. In the SBRT method, the largest difference for the LoS condition is Rx1, which has an RSSI difference of -21.99 dBm compared to the measurement result. In the APSM method, the largest RSSI difference that can be observed is Rx6 which has a -6.44 dBm difference. This might be caused by the large number of interactions received by Rx6 due to the reflection and diffractions encountered at the sharp edge of the Room 1 wall. Other receivers show good agreement with the measurement result, especially Rx4 which only has a -0.65 dBm RSSI difference.

Rx17 to Rx33 demonstrates the distance relationship of RSSI in NLoS scenario. The overall RSSI is higher than LoS condition due to lesser rays received directly but with a higher number of interactions. In the SBRT method, Rx23 shows the largest difference of RSSI of 18.39 dBm whereas, in APSM, the largest RSSI difference of -23.36 dBm can be seen from Rx30. This is due to the high number of obstacles encountered by Rx30 such as door, concrete wall, ceiling, and floor. Rx34 to Rx37 demonstrate the Room 3 scenario. The proposed APSM achieved higher accuracy with the largest and smallest RSSI differences of -6.29 dBm and 0.66 dBm, respectively. In-Room 1, Rx38 to Rx46 are placed to measure RSSI. SBRT method has the largest RSSI difference of -34.61 dBm at Rx45, wherein APSM only differs by -3.31 dBm for the same receiver. The overall RSSI level for Rx38 to Rx46 is lower, due to the concrete wall being the only obstacle encountered by the rays since Tx is placed outside Room 1. In Room 4, the largest RSSI difference is shown by Rx48 for

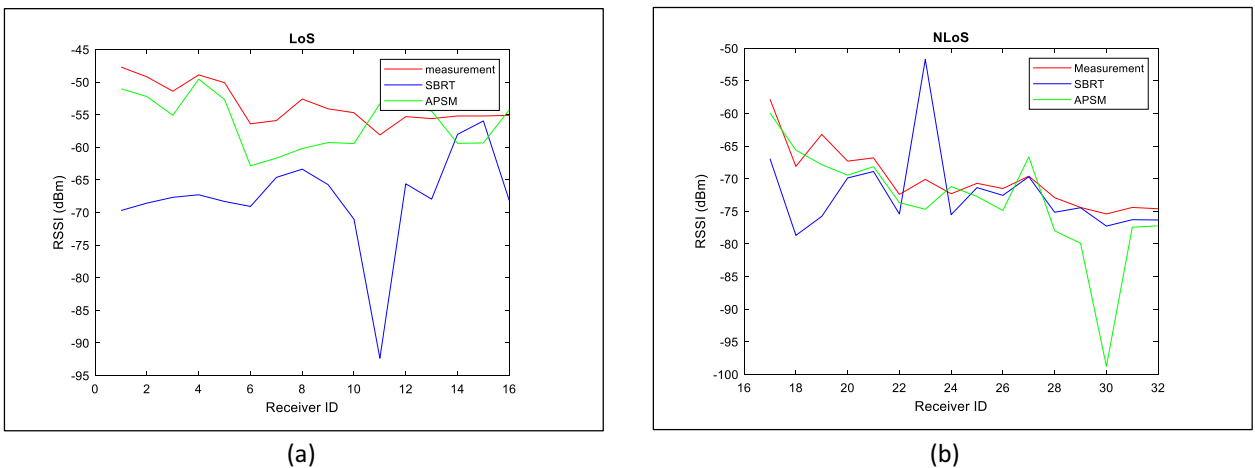


Fig. 6 RSSI data for measurement campaign (section IV-A), SBRT method and APSM method implemented in the simulation at 4.5 GHz (section IV-B) (a) LoS and (b) NLoS.

Table 3 SIMULATION RESULT AT 4.5GHZ.

	Receiver ID	Measurement RSSI (dBm)	SBRT Method RSSI (dBm)	APSM Method RSSI (dBm)
LoS	Rx1	-47.70	-69.69	-51.03
	Rx2	-49.20	-68.56	-52.22
	Rx3	-51.40	-67.67	-55.09
	Rx4	-48.90	-67.28	-49.55
	Rx5	-50.10	-68.31	-52.68
	Rx6	-56.40	-69.07	-62.84
	Rx7	-55.90	-64.62	-61.67
	Rx8	-52.60	-63.36	-60.19
	Rx9	-54.10	-65.73	-59.27
	Rx10	-54.70	-71.03	-59.42
	Rx11	-58.10	-92.35	-53.32
	Rx12	-55.30	-65.60	-53.87
	Rx13	-55.60	-67.95	-54.45
	Rx14	-55.20	-58.02	-59.4
	Rx15	-55.20	-55.96	-59.33
	Rx16	-55.10	-68.16	-54.24
NLoS	Rx17	-57.80	-66.92	-59.93
	Rx18	-68.10	-78.68	-65.61
	Rx19	-63.20	-75.77	-67.84
	Rx20	-67.30	-69.88	-69.45
	Rx21	-66.80	-68.89	-68.15
	Rx22	-72.40	-75.41	-73.67
	Rx23	-70.10	-51.71	-74.68
	Rx24	-72.30	-75.51	-71.19
	Rx25	-70.70	-71.36	-72.72
	Rx26	-71.50	-72.55	-74.87
Rx27	-69.60	-69.69	-66.65	
Rx28	-72.90	-75.14	-77.98	
Rx29	-74.40	-74.44	-79.89	
Rx30	-75.40	-77.26	-98.76	
Rx31	-74.40	-76.28	-77.43	
Rx32	-74.60	-76.32	-77.22	
Rx33	-76.70	-78.65	-79.56	
Room 3	Rx34	-56.80	-60.52	-55.67
	Rx35	-60.70	-61.59	-66.99
	Rx36	-66.00	-68.02	-65.34
	Rx37	-77.40	-77.60	-79.98
Room 1	Rx38	-45.70	-59.36	-49.33
	Rx39	-55.40	-57.33	-59.12
	Rx40	-53.00	-56.06	-59.43
	Rx41	-49.80	-64.79	-46.45
	Rx42	-51.40	-64.61	-53.29
	Rx43	-56.10	-56.47	-52.33
	Rx44	-53.30	-63.48	-59.66
	Rx45	-53.50	-88.11	-56.81
	Rx46	-51.60	-58.50	-55.33
	Room 4	Rx47	-55.40	-56.69
Rx48		-55.30	-83.16	-52.54
Rx49		-61.90	-63.17	-66.44
Rx50		-51.00	-70.17	-55.56
Rx51		-54.80	-68.15	-52.33
Rx52		-57.60	-49.71	-56.56
Rx53		-53.60	-61.35	-52.33
Rx54		-57.70	-59.16	-57.55
Rx55		-57.80	-62.06	-57.44
Rx56		-57.40	-64.35	-58.67
Rx57		-57.50	-62.09	-55.76
Rx58		-59.90	-55.03	-56.33
Rx59		-57.80	-59.09	-56.29
Rx60		-61.60	-69.57	-65.56

Table 3 (continued)

	Receiver ID	Measurement RSSI (dBm)	SBRT Method RSSI (dBm)	APSM Method RSSI (dBm)
Room 2	Rx61	-49.80	-55.75	-45.67
	Rx62	-45.90	-58.55	-45.76
	Rx63	-51.80	-73.20	-44.56
	Rx64	-51.40	-62.91	-50.33
	Rx65	-55.30	-62.26	-55.33
Room 6	Rx66	-56.80	-59.61	-56.99
	Rx67	-59.30	-63.32	-56.22
	Rx68	-59.50	-63.68	-57.2
	Rx69	-58.90	-62.88	-56.34
	Rx70	-57.50	-71.73	-55.78
	Rx71	-54.30	-57.41	-51.44
Room 5	Rx72	-57.00	-63.57	-56.56
	Rx73	-66.20	-69.22	-65.44
	Rx74	-66.40	-69.71	-68.62
	Rx75	-65.20	-68.11	-67.6
	Rx76	-60.00	-63.53	-59.78
	Rx77	-53.00	-63.83	-56.35
	Rx78	-52.80	-56.48	-52.32
	Rx79	-54.20	-72.41	-51.34
	Rx80	-67.20	-79.41	-62.78
	Rx81	-69.60	-87.70	-68.83
	Rx82	-71.50	-77.65	-69.89
	Rx83	-74.80	-81.13	-78.51

the SBRT method, while in APSM it is shown in Rx50 which has -4.56 dBm.

In Room 2, SBRT shows the average difference of -11.694 dBm whereas APSM shows the average difference of only 2.51 dBm. For Room 6, Rx70 shows the largest RSSI difference of -14.23 dBm since it is placed at the centre of the hall. In APSM, Rx66, Rx74, Rx75 and Rx77 have the best RSSI representation corresponding to measurement results. Lastly, in Room 5, APSM also demonstrates good alignment to measurement data with an average difference of 0.7725 dBm, compared to -10.6975 dBm in SBRT. Fig. 7. shows the comparison of APSM and SBRT corresponding to measurement RSSI at 4.5 GHz.

B. Results for 28 GHz

Fig. 8 (a) and (b) show the 2-D and 3-D layouts of SBRT method simulations at 28 GHz, respectively. Similarly, 2-D and 3-D layouts for the APSM simulation at the same frequency are shown in Fig. 8 (c) and (d).

Fig. 9 shows the RSSI data obtained from the measurement campaign (section IV-A), SBRT method, and APSM method implemented in the simulation (section IV-B) at 28 GHz for the LoS and NLoS scenarios and presented in Table 4 for all scenarios.

Table 4 shows the RSSI data obtained from the measurement campaign (section V-A), SBRT method, and APSM method implemented in the simulation (section V-B) at 28 GHz. The mean RSSI from measurement is -75.77 dBm. In the SBRT method, the mean RSSI is -87.17 dBm while in the proposed APSM it is -77.69 dBm. The average RSSI difference derived from the table is -11.41 dBm in SBRT and -1.93 dBm in APSM. The overall simulation result in the proposed APSM is more accurate since it has a lower error

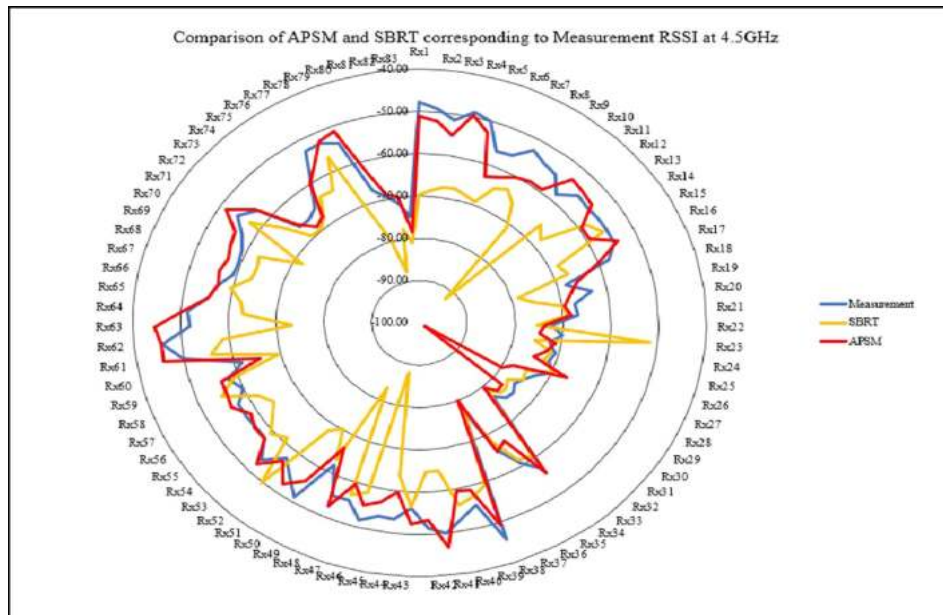


Fig. 7 Comparison of APSM and SBRT corresponding to Measurement RSSI at 4.5 GHz.

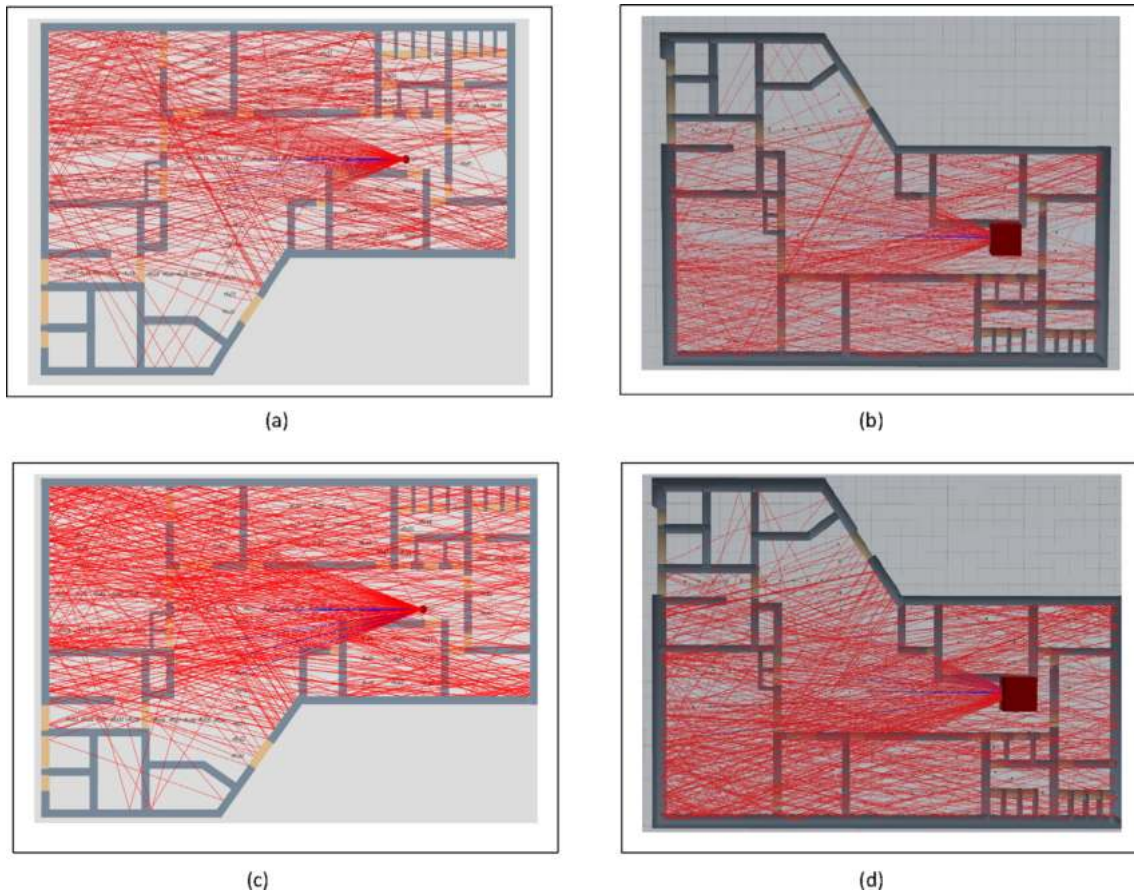


Fig. 8 (a) 2-D Layout of SBRT Method after simulation at 28 GHz, (b) 3-D Layout of SBRT Method after simulation at 28 GHz, (c) 2-D Layout of APSM after simulation at 28 GHz, (d) 3-D Layout of APSM after simulation at 28 GHz.

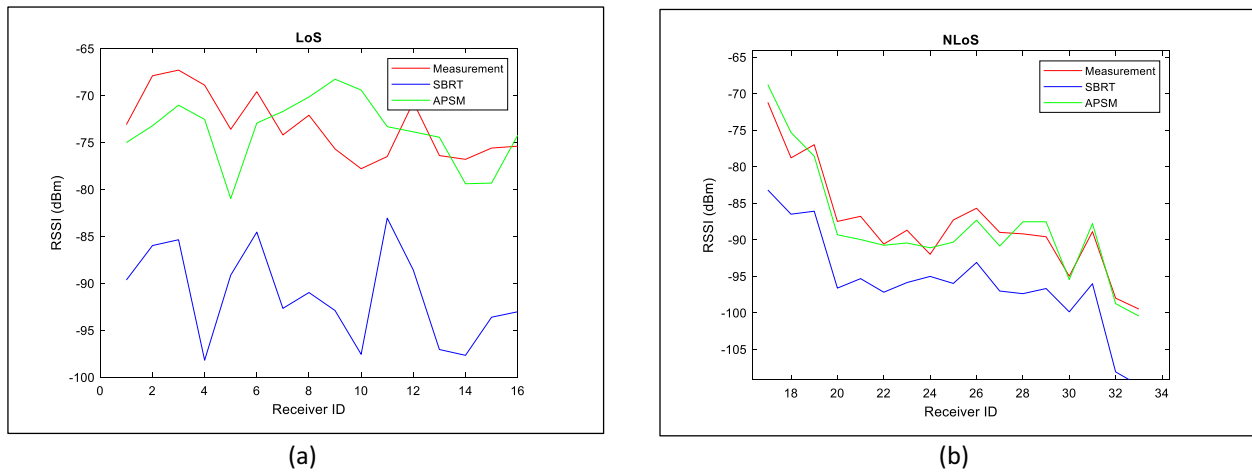


Fig. 9 RSSI data for measurement campaign (section IV-A), SBRT method and APSM method implemented in the simulation at 28 GHz (section IV-B) (a) LoS and (b) NLoS.

Table 4 SIMULATION RESULT AT 28 GHZ.

	Receiver ID	Measurement RSSI (dBm)	SBRT Method RSSI (dBm)	APSM Method RSSI (dBm)	
LoS	Rx1	-57.90	-82.01	-59.32	
	Rx2	-55.10	-81.14	-60.43	
	Rx3	-56.90	-78.92	-58.11	
	Rx4	-59.50	-79.63	-58.45	
	Rx5	-58.60	-92.05	-61.33	
	Rx6	-66.50	-93.59	-67.28	
	Rx7	-58.80	-85.59	-62.99	
	Rx8	-61.40	-79.69	-63.76	
	Rx9	-67.80	-112.18	-68.34	
	Rx10	-66.50	-97.74	-68.23	
	Rx11	-77.90	-87.89	-78.34	
	Rx12	-70.30	-79.61	-72.54	
	Rx13	-69.10	-79.1	-71.33	
	Rx14	-66.00	-85.16	-67.49	
	Rx15	-64.10	-81.83	-68.34	
NLoS	Rx16	-63.40	-81.9	-65.45	
	Rx17	-71.20	-83.2	-68.78	
	Rx18	-78.80	-86.51	-75.33	
	Rx19	-77.00	-86.1	-78.56	
	Rx20	-87.50	-96.63	-89.33	
	Rx21	-86.80	-95.33	-89.98	
	Rx22	-90.60	-97.19	-90.76	
	Rx23	-88.70	-95.87	-90.45	
	Rx24	-92.00	-95.03	-91.11	
	Rx25	-87.30	-95.99	-90.34	
	Rx26	-85.70	-93.12	-87.33	
	Rx27	-89.00	-97.03	-90.87	
	Rx28	-89.20	-97.39	-87.55	
	Rx29	-89.60	-96.69	-87.55	
	Rx30	-95.00	-99.88	-95.45	
	Rx31	-88.90	-96.03	-87.78	
	Rx32	-98.00	-108.1	-98.76	
	Rx33	-99.50	-109.93	-100.45	
	Room 3	Rx34	-74.20	-97.73	-77.67
		Rx35	-75.60	-95.03	-78.77
		Rx36	-67.80	-87.54	-69.91
		Rx37	-91.00	-98.61	-92.67

Table 4 (continued)

	Receiver ID	Measurement RSSI (dBm)	SBRT Method RSSI (dBm)	APSM Method RSSI (dBm)	
Room 1	Rx38	-55.40	-73.93	-59.89	
	Rx39	-67.50	-78.56	-68.45	
	Rx40	-72.60	-81.16	-78.50	
	Rx41	-66.50	-75.02	-67.90	
	Rx42	-61.60	-69.19	-67.56	
	Rx43	-59.00	-68.23	-61.44	
	Rx44	-73.80	-76.21	-75.44	
	Rx45	-68.20	-79.26	-71.67	
	Rx46	-64.30	-76.61	-67.56	
	Room 4	Rx47	-69.80	-74.55	-70.12
		Rx48	-74.10	-83.39	-72.23
Rx49		-79.80	-89.62	-81.12	
Rx50		-67.10	-80.06	-69.76	
Rx51		-80.50	-76.55	-83.67	
Rx52		-80.70	-79.59	-81.45	
Rx53		-71.90	-75.56	-75.56	
Rx54		-70.20	-74.12	-73.45	
Rx55		-79.20	-84.74	-84.33	
Rx56		-77.70	-80.96	-79.67	
Room 2	Rx57	-78.40	-79.57	-80.33	
	Rx58	-61.00	-62.41	-63.45	
	Rx59	-76.00	-96.11	-79.67	
	Rx60	-76.40	-95.94	-78.54	
	Rx61	-64.40	-77.28	-67.34	
	Rx62	-60.00	-70.59	-64.37	
	Rx63	-67.10	-77.59	-68.33	
	Rx64	-60.30	-71.03	-66.78	
	Rx65	-65.80	-77.93	-67.67	
	Room 6	Rx66	-75.70	-89.26	-77.67
Rx67		-79.20	-91.08	-81.78	
Rx68		-76.40	-90.01	-76.89	
Rx69		-69.90	-82.65	-70.34	
Rx70		-76.10	-87.17	-78.78	
Rx71		-74.50	-85.54	-75.67	
Rx72		-79.30	-91.63	-81.56	
Rx73		-90.30	-92.36	-95.87	
Rx74		-93.50	-99.12	-97.67	

Table 4 (continued)

	Receiver ID	Measurement RSSI (dBm)	SBRT	APSM
			Method RSSI (dBm)	Method RSSI (dBm)
	Rx75	-90.50	-95.65	-92.45
	Rx76	-89.20	-96.47	-90.54
	Rx77	-82.90	-94.69	-84.37
	Rx78	-80.00	-93.33	-83.66
	Rx79	-80.80	-91.81	-81.45
Room	Rx80	-94.70	-96.74	-94.56
5	Rx81	-92.10	-92.19	-93.45
	Rx82	-94.90	-96.5	-95.78
	Rx83	-96.10	-96.39	-98.56

percentage of 2.53 % compared to the conventional SBRT method which has a 15.05 % error. APSM has achieved a 61.93 % reduction with only 24,672 rays launched, compared to 64,800 rays launched in SBRT. In terms of time taken for simulation, APSM takes 7425.55 ms to launch all the rays compared to 23317.4419 ms taken in the SBRT method. In the other words, APSM is 68.15 % faster than the conventional method at 28 GHz.

Similarly, in section V-A, Rx1 to Rx16 are placed to represent LoS scenario. The largest RSSI difference in SBRT can be seen in Rx9 with -44.38 dBm, whereby the difference is reduced effectively in APSM with -0.54 dBm difference. The closest values in Room 1 are -9.31 dBm by Rx12 and -0.44 dBm by Rx11, for SBRT and APSM, respectively. For the NLoS scenario, all the receivers in APSM have good alignment to the measured RSSI compared to the SBRT method, whereby in SBRT Rx17, Rx32 and Rx33 have high differences

of -12.00 dBm, -10.10 dBm, and -10.43 dBm, respectively. The RSSI value is quite high in Room 3 due to the many obstacles and wall partitions that separate the rooms. This is reduced in APSM in which the lowest difference of -1.67 dBm is achieved by Rx37. In-Room 1, Rx38 shows the high RSSI difference of -18.53 dBm, but it is reduced to -4.49 dBm in APSM for the same receiver. Similarly, APSM also aligns better than SBRT by reducing the RSSI difference from -12.96 dBm to -2.66 dBm at Rx50, -20.11dBm to -3.67 dBm at Rx59, and -19.54dBm to -2.14 dBm at Rx51. In-Room 2, the average RSSI difference is -11.364 dBm, while APSM improves it to -3.378 dBm. The fluctuations in RSSI difference in Room 6 through SBRT also minimize in APSM with the highest difference of -4.17 dBm at Rx74 and lowest difference of -0.44 dBm at Rx69. Lastly, in Room 5, the improvement is less significant in APSM with an average difference of -1.129 dBm, compared to -1.005 dBm in SBRT. Fig. 10 shows the comparison of the APSM and SBRT corresponding to measurement RSSI at 28 GHz.

C. Results for 38 GHz

Fig. 11 (a) and (b) show the 2-D and 3-D layouts of SBRT method simulations at 38 GHz, respectively. Similarly, 2-D and 3-D layouts for the APSM simulation at the same frequency are shown in Fig. 8 (c) and (d).

Fig. 12 shows the RSSI data obtained from the measurement campaign (section IV-A), SBRT method, and APSM method implemented in the simulation (section IV-B) at 38 GHz for the LoS and NLoS scenarios and presented in Table 5 for all scenarios.

Table 5 shows the RSSI data obtained from the measurement campaign (section IV-A), SBRT method, and APSM

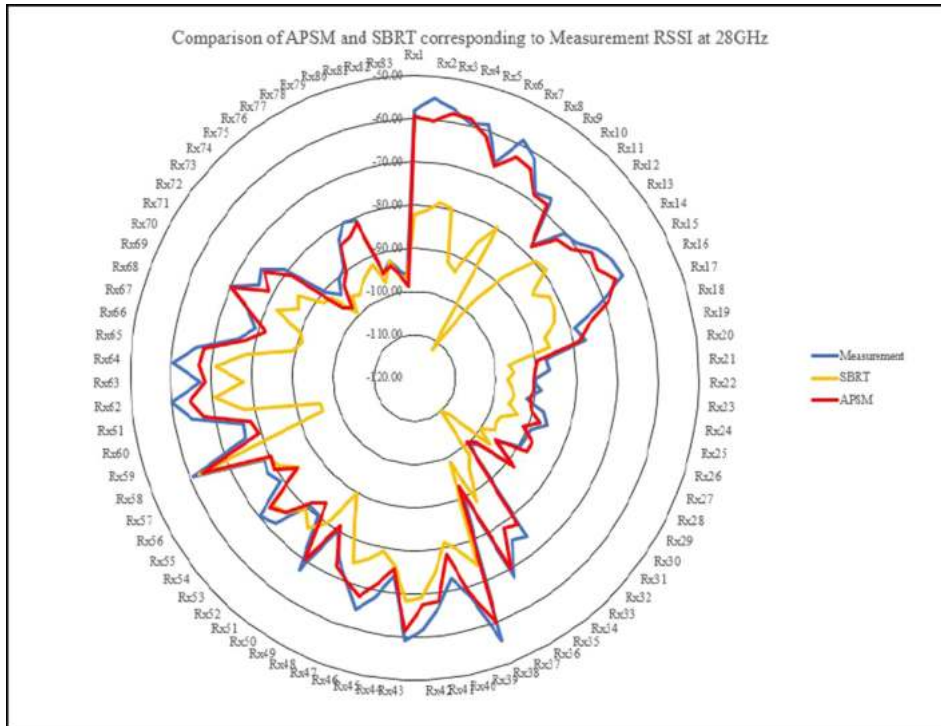


Fig. 10 Comparison of APSM and SBRT corresponding to RSSI Measurement at 28 GHz.

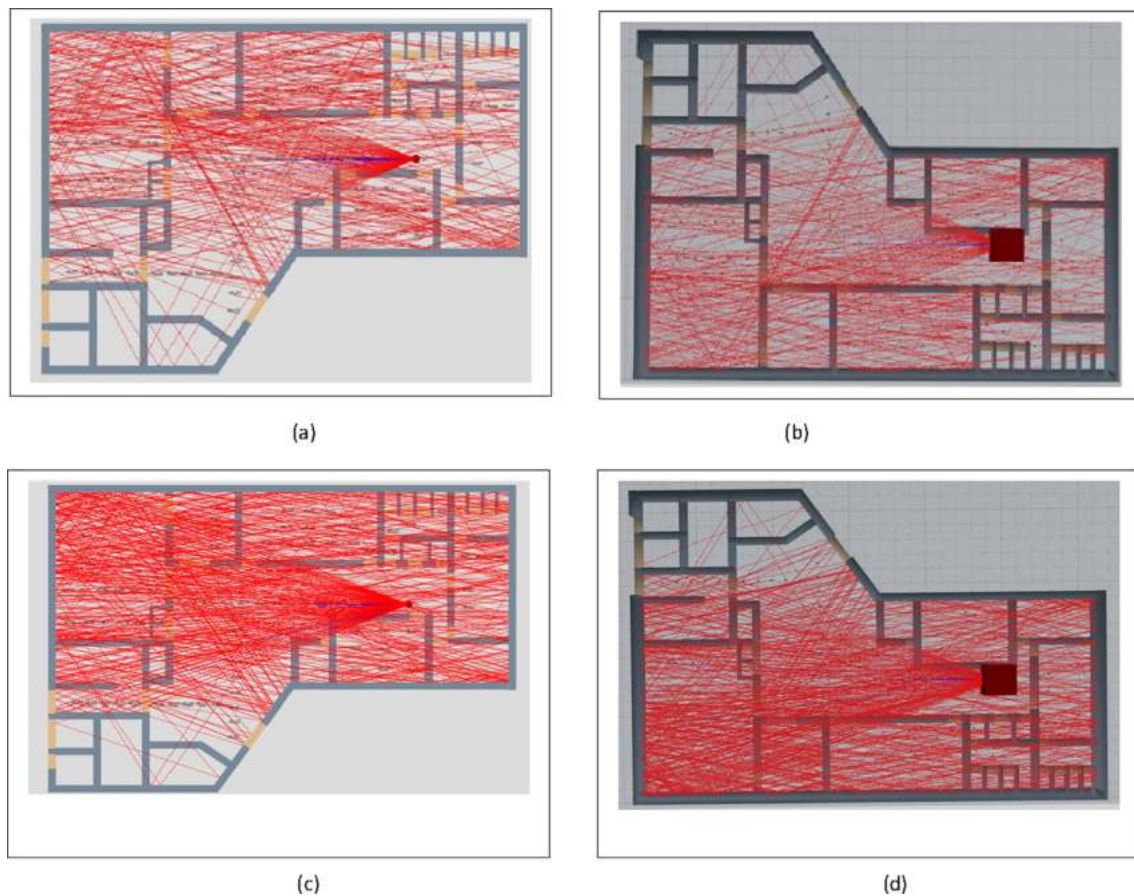


Fig. 11 (a) 2-D Layout of SBRT Method after simulation at 38 GHz, (b) 3-D Layout of SBRT Method after simulation at 38 GHz, (c) 2-D Layout of APSM after simulation at 38 GHz, (d) 3-D Layout of APSM after simulation at 38 GHz.

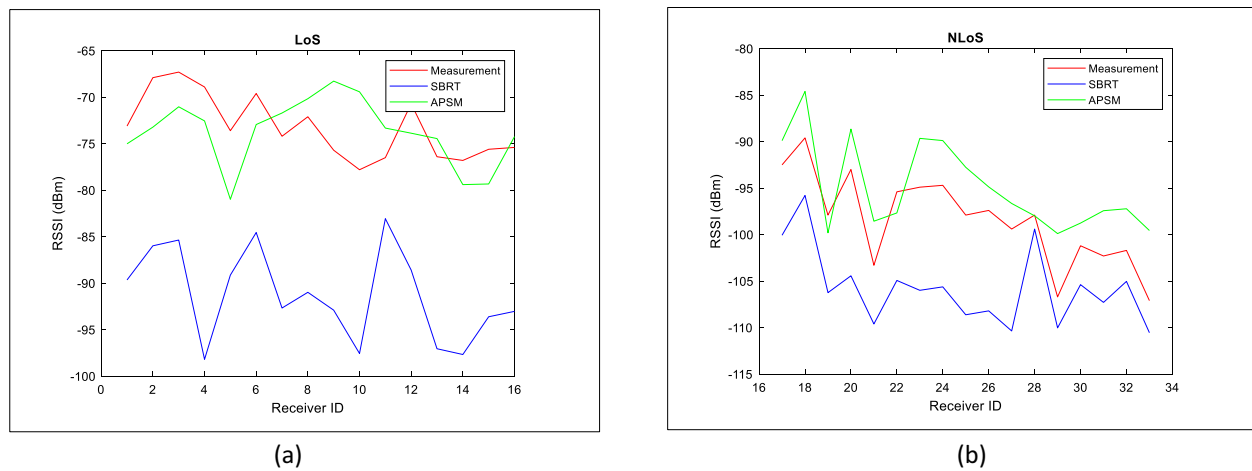


Fig. 12 RSSI data for measurement campaign (section IV-A), SBRT method and APSM method implemented in the simulation at 38 GHz (section IV-B) (a) LoS and (b) NLoS.

method implemented in the simulation (section IV-B) at 38 GHz. The mean RSSI from measurement is -85.68 dBm. The mean RSSI in the SBRT method is -95.14 dBm with an average RSSI difference of -9.45 dBm, compared to measurement data. Conversely, the proposed APSM method has a

mean RSSI of -84.32 dBm with an average RSSI difference of 1.36 dBm compared to the measurement result. For 38 GHz cases, the percentage of error in APSM is also lower compared to the conventional SBRT method. For example, APSM achieved a 1.59% error corresponding to measured

Table 5 SIMULATION RESULT AT 38 GHz

	Receiver ID	Measurement RSSI (dBm)	SBRT Method RSSI (dBm)	APSM Method RSSI (dBm)
LoS	Rx1	-73.10	-89.65	-75.01
	Rx2	-67.90	-85.98	-73.22
	Rx3	-67.30	-85.36	-71.03
	Rx4	-68.90	-98.19	-72.55
	Rx5	-73.60	-89.13	-80.98
	Rx6	-69.60	-84.55	-72.94
	Rx7	-74.20	-92.67	-71.7
	Rx8	-72.10	-90.98	-70.16
	Rx9	-75.70	-92.9	-68.27
	Rx10	-77.80	-97.56	-69.42
	Rx11	-76.50	-83.06	-73.32
	Rx12	-70.70	-88.59	-73.87
	Rx13	-76.40	-97.05	-74.45
	Rx14	-76.80	-97.67	-79.4
	Rx15	-75.60	-93.61	-79.33
	Rx16	-75.40	-93.03	-74.24
NLoS	Rx17	-92.50	-100.07	-89.9
	Rx18	-89.60	-95.79	-84.6
	Rx19	-97.90	-106.24	-99.81
	Rx20	-93.00	-104.43	-88.65
	Rx21	-103.30	-109.61	-98.56
	Rx22	-95.40	-104.93	-97.67
	Rx23	-94.90	-105.99	-89.65
	Rx24	-94.70	-105.62	-89.89
	Rx25	-97.90	-108.62	-92.76
	Rx26	-97.40	-108.2	-94.87
	Rx27	-99.40	-110.36	-96.65
	Rx28	-97.90	-99.4	-97.98
	Rx29	-106.70	-110.03	-99.89
	Rx30	-101.20	-105.38	-98.76
Rx31	-102.30	-107.29	-97.43	
Rx32	-101.70	-105.03	-97.22	
Rx33	-107.10	-110.55	-99.56	
Room 3	Rx34	-83.60	-95.46	-85.67
	Rx35	-89.90	-100.44	-86.9
	Rx36	-86.60	-97.13	-85.34
	Rx37	-108.30	-108.62	-99.98
Room 1	Rx38	-72.20	-76.94	-79.33
	Rx39	-78.20	-82.7	-79.67
	Rx40	-82.80	-86.68	-79.97
	Rx41	-75.20	-79.1	-76.66
	Rx42	-69.60	-78.06	-73.29
	Rx43	-73.00	-83.55	-72.33
	Rx44	-85.20	-91.81	-79.66
	Rx45	-75.40	-79.1	-76.81
	Rx46	-76.80	-80.18	-75.33
Room 4	Rx47	-81.90	-88.66	-79.66
	Rx48	-84.50	-91.09	-82.54
	Rx49	-89.60	-93.79	-86.44
	Rx50	-77.00	-86.54	-75.56
	Rx51	-85.50	-92.2	-82.33
	Rx52	-89.80	-95.39	-86.56
	Rx53	-79.50	-84.45	-82.33
	Rx54	-71.00	-78.64	-70.55
	Rx55	-90.10	-96.11	-89.44
	Rx56	-78.80	-91.21	-78.67
	Rx57	-79.70	-85.91	-75.76
	Rx58	-77.40	-83.47	-76.33
	Rx59	-87.40	-92.11	-86.29
	Rx60	-86.10	-93.25	-85.56

Table 5 (continued)

	Receiver ID	Measurement RSSI (dBm)	SBRT Method RSSI (dBm)	APSM Method RSSI (dBm)
Room 2	Rx61	-79.60	-84.7	-75.67
	Rx62	-65.30	-81.36	-60.76
	Rx63	-75.40	-87.04	-74.56
	Rx64	-68.80	-77.06	-70.33
	Rx65	-72.40	-85.31	-75.33
Room 6	Rx66	-90.50	-99.93	-86.99
	Rx67	-87.00	-98.74	-86.22
	Rx68	-89.10	-99.42	-87.2
	Rx69	-84.10	-87.61	-86.34
	Rx70	-83.60	-90.76	-85.78
	Rx71	-81.90	-93.93	-81.44
	Rx72	-88.20	-89.69	-86.56
	Rx73	-98.40	-99.5	-95.44
	Rx74	-102.40	-113.32	-98.67
Room 5	Rx75	-99.20	-112.17	-97.6
	Rx76	-94.90	-101.99	-96.78
	Rx77	-97.30	-111.28	-96.34
	Rx78	-95.00	-103.52	-92.34
	Rx79	-94.10	-98.15	-91.32
	Rx80	-99.80	-106.56	-92.76
	Rx81	-102.00	-110.41	-98.89
	Rx82	-106.10	-113.77	-99.89
	Rx83	-97.00	-99.91	-98.56

RSSI, while SBRT has a percentage error as high as 11.04 %. In terms of the launched ray, APSM improves the ray-tracing by 63.96 % since the proposed method reduces the number of rays launched from 64,800 in SBRT to 23352. APSM also reduces computational time with only 7320.55 ms required for the whole ray-tracing simulation, whereby the SBRT method requires 10321.55 ms.

The power level in terms of RSSI decreases in 38 GHz compared to 4.5 GHz and 28 GHz. In LOS condition, Rx4 possesses the largest RSSI difference of -29.29 dB in the SBRT method, while this is improved in APSM with only -3.65 dBm difference. Most of the Rx have a close alignment with the measured RSSI except Rx9 and Rx10, while the receivers may not receive all the rays due to shorter paths travelling at a high 38 GHz frequency. In NLoS scenario, APSM has achieved the maximum RSSI difference of 6.81 dBm at Rx29 and a minimum of -0.08 dBm at Rx28. Meanwhile, in SBRT, Rx20 has the largest RSSI difference at -11.43 dBm and the smallest of -1.50 dBm at Rx28. APSM also reduces the average RSSI difference in Room 3, from -8.3125 dBm to 2.6275 dBm. In-Room 1, SBRT has the largest RSSI difference at Rx43 with -10.55 dBm, while APSM only has the largest deviation of -7.13 dBm at Rx38. Similarly, in Room 4, all the receivers especially Rx54, Rx55, Rx56, and Rx60 have the closest RSSI value corresponding to measured RSSI with less than a dBm difference. For Room 2, there is also a significant improvement of the average received power level difference from -10.794 dBm in SBRT to 0.952 dBm. In-Room 6, SBRT has large RSSI difference at Rx67, Rx68, Rx71, Rx74, Rx75 and Rx77, namely, -11.74dBm, -10.32dBm, -12.03dBm, -10.92dBm and -13.98dBm, respectively All these deviations have been reduced effectively to 0.78dBm, 1.90dBm, 0.46dBm,

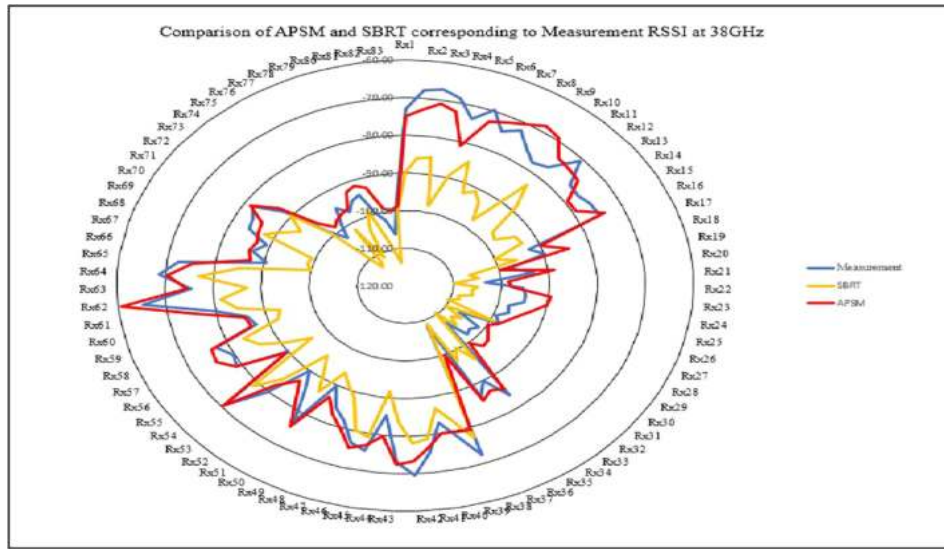


Fig. 14 Comparison of APSM and SBRT corresponding to Measurement RSSI at 38 GHz.

Table 6 SUMMARY OF MEASUREMENT, SBRT AND APSM RESULT

Frequency (GHz)	4.5		
Method	Measurement	SBRT	APSM
Mean (dBm)	-59.54	-67.25	-60.85
Average RSSI Difference (dBm)	-	-7.71	-1.31
Total Number of Ray Launched	-	3240	1412
Time taken (ms)	-	23317.4419	7620.55
Frequency (GHz)	28		
Method	Measurement	SBRT	APSM
Mean (dBm)	-75.77	-87.17	-77.69
Average RSSI difference (dBm)	-	-11.41	-1.93
Total number of rays launched.	-	3240	1329
Time taken (ms)	-	23317.4419	7425.55
Frequency (GHz)	38		
Method	Measurement	SBRT	APSM
Mean (dBm)	-85.68	-95.14	-84.32
Average RSSI difference (dBm)	-	-9.45	1.36
Total number of rays launched	-	3240	1246
Time taken (ms)	-	10321.5555	7320.55

3.73dBm and 0.96dBm, respectively, in APSM. Lastly, in Room 5, APSM improves the ray tracing process from an average of -6.4375 dBm to 3.7 dBm.

Fig. 14 shows the comparison of the APSM and SBRT corresponding to measurement RSSI at 38 GHz.

D. Complexity Analysis of Proposed Method

In the proposed APSM, the rays have been predefined to a specific direction compared to the conventional SBRT method which shoots the rays randomly, therefore the proposed method greatly reduces the computational complexity and time. The simulation time, T , in APSM can be simplified by Eq. (19).

$$T = t \times \left[\left(\frac{\theta_H}{\Delta\varphi} \times \frac{\theta_V}{\Delta\theta} \right) + 4n \right] \quad (19)$$

Here, θ_H is the horizontal angle range of launching ray, θ_V is the vertical angle range of launching ray, $\Delta\varphi$ is the horizontal angle step size of launching ray, $\Delta\theta$ is the vertical angle step size of launching ray, t is the average simulation time for single ray, and n is the number of successive directions in Step III (refer to section III). In this research, θ_H is set from 157.5° to 175.5°, covering the range of 18°. $\Delta\varphi$ is $\pi/60$ which effectively reduces the number of launching rays compared to the conventional method. The summary of the results is shown in Table 6.

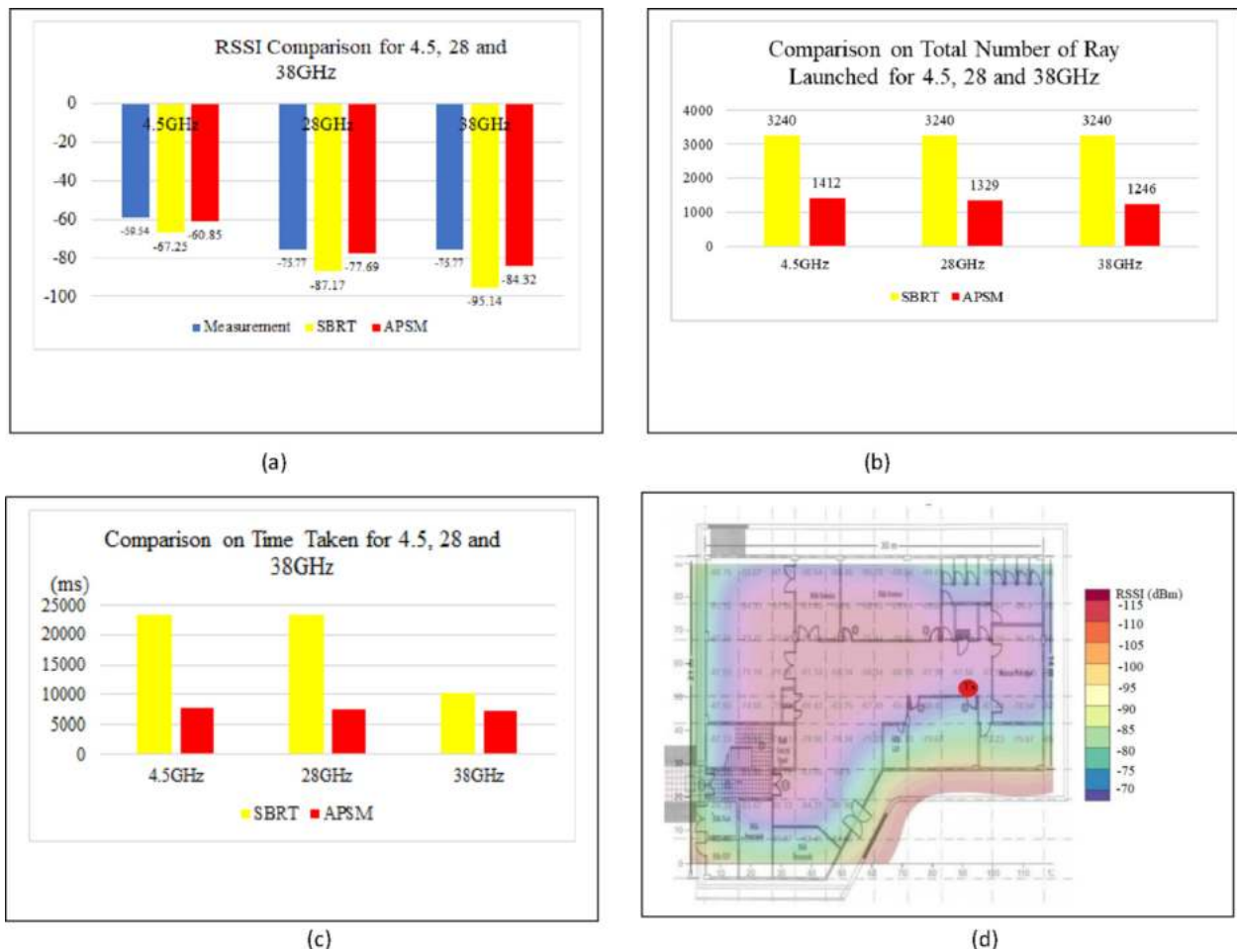


Fig. 15 (a) Comparison of mean RSSI for APMS and SBRT corresponding to Measurement at 4.5, 28 and 38 GHz, (b) Comparison of the number of rays for APMS and SBRT at 4.5, 28 and 38 GHz, (c) Comparison of time taken in APMS and SBRT at 4.5, 28 and 38 GHz (d) Contour plot mapped to WCC block P15a building layout at 4.5 GHz.

The RSSI comparison in Fig. 15. (a) demonstrated the robustness of APMS based on measurement concerning SBRT. The number of ray launching is greatly reduced for APMS in Fig. 15. (b) with a different frequency as ray launch predefined specific direction which reduces the complexity concerning SBRT. Fig. 15. (c) demonstrated the important milestones to ray tracing technology based on simulation time of APMS compare to the SBRT. Finally, the APMS method reduced the complexity of ray tracing in the field of radio propagation prediction.

7. Conclusion

In this article, APMS is proposed at 4.5 GHz, 28 GHz, and 38 GHz to investigate indoor radio propagation for potential communication system development. A measurement campaign has been conducted to obtain the data in terms of RSSI. The APMS has been evaluated along with the conventional SBRT method with the same building layout where the measurement is conducted. In contrast to other works where walls were considered as the only obstacles, the attenuation from the

ceiling and floor were accounted for in this work, for a more realistic building layout modeling. Power levels in terms of RSSI obtained from APMS and SBRT are compared to the measurement result. The comparison results show that the APMS achieves higher RSSI accuracy compared to SBRT. APMS has effectively minimized the computational resources and time needed by 60 %, without reducing the valid ray paths between Tx and Rx at 4.5 GHz, 28 GHz, and 38 GHz. For future work, the APMS can be extended to outdoor radio wave propagation. More research is needed for further improvement in the speed and accuracy of the APMS in a crowded scenario. The Multiple-Input and Multiple-Output system can be implemented through the APMS simulation. Implementing the APMS in multiple cell and further research can be a very good solution for 5G network planning.

Declaration of Competing Interest

The authors declare that they have no known competing financial interests or personal relationships that could have appeared to influence the work reported in this paper.

Acknowledgement

Special thanks to Multimedia University (MMU), Melaka, Malaysia and Telekom Malaysia Berhad, Malaysia. Thanks also to Kementerian Pengajian Tinggi (KPT) Malaysia for supporting the project title “Indoor Internet of Things (IOT) Tracking Algorithm Development based on Radio Signal Characterisation” (grant no. FRGS/1/2018/TK08/MMU/02/1) for financial support. This work was supported in part by KPT and Universiti Teknologi Malaysia (UTM) under the research Grant, Q.J130000.21A2.5F237, 4B536, 00L47 and 01M98.

References

- [1] G. Xu, IoT-assisted ECG monitoring framework with secure data transmission for health care applications, *IEEE Access* 8 (2020) 74586–74594.
- [2] P. Gandotra, R.K. Jha, A survey on green communication and security challenges in 5G wireless communication networks, *Journal of Network and Computer Applications* 96 (2017) 39–61.
- [3] L. Chettri, R. Bera, A comprehensive survey on Internet of Things (IoT) toward 5G wireless systems, *IEEE Internet of Things Journal* 7 (2020) 16–32.
- [4] F. Casino, L. Azpilicueta, P. Lopez-Iturri, E. Aguirre, F. Falcone, A. Solanas, Optimized wireless channel characterization in large complex environments by hybrid ray launching-collaborative filtering approach, *IEEE Antennas and Wireless Propagation Letters* 16 (2017) 780–783.
- [5] I.R. Gomes, C.R. Gomes, H.S. Gomes, G.P.D.S. Cavalcante, Empirical radio propagation model for DTV applied to non-homogeneous paths and different climates using machine learning techniques, *PLoS one* 13 (3) (2018).
- [6] C.V. Forecast, “Cisco visual networking index: global mobile data traffic forecast update, 2016–2021 white paper”, Cisco Public, Information (2017).
- [7] T. Imai, A survey of efficient ray-tracing techniques for mobile radio propagation analysis, *IEICE Transactions on Communications* (2016).
- [8] M.M. Taygur, T.F. Eibert, A ray-tracing algorithm based on the computation of (exact) ray paths with bidirectional ray-tracing, *IEEE Transactions on Antennas and Propagation* 68 (2020) 6277–6286.
- [9] S. Mercader-Pellicer, G. M. Mederò and G. Goussetis, “Comparison of geometrical and physical optics for cross-polarisation prediction in reflector antennas,” in *Active and Passive RF Devices* (2017), 2017.
- [10] P. Hamel, J. Adam, G. Kubické and P. Pouliguen, “An improved hybridization technique of geometrical optics physical optics,” in *2012 15 International Symposium on Antenna Technology and Applied Electromagnetics*, 2012.
- [11] H. Shirai, R. Sato, K. Otoi, Electromagnetic wave propagation estimation by 3-D SBR method, in *2007 International Conference on Electromagnetics in Advanced Applications*, 2007.
- [12] Y.Z. Umul, Uniform asymptotic theory for the edge diffraction of cylindrical waves, *IET Microwaves, Antennas Propagation* 11 (2017) 2219–2222.
- [13] K. Klionovski, S.E. Bankov, A. Shamim, Synthesis of reflectors characterized by the spatial dispersion of the reflection coefficient, *IEEE Open Journal of Antennas and Propagation* 1 (2020) 419–425.
- [14] N.M. Grebenikova, N.S. Myazin, V.Y. Rud’, R.V. Davydov, Monitoring of flowing media state by refraction phenomenon, in *2018 IEEE International Conference on Electrical Engineering and Photonics (EExPolytech)*, 2018.
- [15] X. Li, Y. Li, B. Li, The diffraction research of cylindrical block effect based on Indoor 45 GHz millimeter wave measurements, *Information* 8 (2017) 50.
- [16] L. Lozano, M.J. Algar, E. García, I. González, F. Cátedra, Efficient combination of acceleration techniques applied to high frequency methods for solving radiation and scattering problems, *Computer Physics Communications* 221 (2017) 28–41.
- [17] S. J. Flores, L. F. Mayorgas and F. A. Jimenez, “Reception algorithms for ray launching modeling of indoor propagation,” in *Proceedings RAWCON 98. 1998 IEEE Radio and Wireless Conference* (Cat. No.98EX194), 1998.
- [18] S.S. Zhekov, Z. Nazneen, O. Franek, G.F. Pedersen, Measurement of attenuation by building structures in cellular network bands, *IEEE Antennas and Wireless Propagation Letters* 17 (2018) 2260–2263.
- [19] W. Xue, Q. Li, X. Hua, K. Yu, W. Qiu, B. Zhou, A new algorithm for indoor RSSI radio map reconstruction, *IEEE Access* 6 (2018) 76118–76125.
- [20] K. Lam, C. Cheung, W. Lee, RSSI-based LoRa localization systems for large-scale indoor and outdoor environments, *IEEE Transactions on Vehicular Technology* 68 (2019) 11778–11791.
- [21] E. Goldoni, A. Savioli, M. Risi and P. Gamba, “Experimental analysis of RSSI-based indoor localization with IEEE 802.15.4,” 2010.
- [22] A. Navarro, D. Guevara, J. Gómez, A proposal to improve ray launching techniques, *IEEE Antennas and Wireless Propagation Letters* 18 (2019) 143–146.
- [23] G. Masetti, J.G.W. Kelley, P. Johnson, J. Beaudoin, A ray-tracing uncertainty estimation tool for ocean mapping, *IEEE Access* 6 (2018) 2136–2144.
- [24] Y. Ning, Y. Hu, X. Cheng, Q. Hao, Y. Cheng, T. Li, X. Tao, Freeform surface graded optimization of deformable mirrors in integrated zoom and image stabilization system through vectorial ray tracing and image point freezing method, *IEEE Photonics Journal* 12 (2020) 1–16.
- [25] S. Grubisic, W.P. Carpes, C.B. Lima, P. Kuo-Peng, Ray-tracing propagation model using image theory with a new accurate approximation for transmitted rays through walls, *IEEE Transactions on Magnetics* 42 (2006) 835–838.
- [26] A. Zamani, S.A. Rezaeieh, K.S. Bialkowski, A.M. Abbosh, Boundary estimation of imaged object in microwave medical imaging using antenna resonant frequency shift, *IEEE Transactions on Antennas and Propagation* 66 (2018) 927–936.
- [27] R. A. Valenzuela, S. Fortune and J. Ling, “Indoor propagation prediction accuracy and speed versus number of reflections in image-based 3-D ray-tracing,” in *VTC ’98. 48th IEEE Vehicular Technology Conference. Pathway to Global Wireless Revolution* (Cat. No.98CH36151), 1998.
- [28] J. Lee, D. Yun, H. Kim, W. Yang, N. Myung, Fast ISAR image formations over multispect angles using the shooting and bouncing rays, *IEEE Antennas and Wireless Propagation Letters* 17 (2018) 1020–1023.
- [29] H. Ling, R. Chou, S. Lee, Shooting and bouncing rays: calculating the RCS of an arbitrarily shaped cavity, *IEEE Transactions on Antennas and Propagation* 37 (1989) 194–205.
- [30] C. Teh, B. Chung, E. Lim, An accurate and efficient 3-D shooting-and-bouncing-polygon ray tracer for radio propagation modeling, *IEEE Transactions on Antennas and Propagation* 66 (2018) 7244–7254.
- [31] D. Yun, J. Lee, K. Bae, J. Yoo, K. Kwon, N. Myung, Improvement in computation time of 3-D scattering center extraction using the shooting and bouncing ray technique, *IEEE Transactions on Antennas and Propagation* 65 (2017) 4191–4199.

- [32] Y. Dama, R. Abd-Alhameed, F. Salazar-Quiñonez, D. Zhou, S. Jones, S. Gao, MIMO indoor propagation prediction using 3D shoot-and-bounce ray (SBR) tracing technique for 2.4 GHz and 5 GHz, in Proceedings of the 5th European Conference on Antennas and Propagation (EUCAP), 2011.
- [33] D. Shi, X. Tang, C. Wang, The acceleration of the shooting and bouncing ray tracing method on GPUs, in 2017 XXXIInd General Assembly and Scientific Symposium of the International Union of Radio Science (URSI GASS), 2017.
- [34] D. Beauvarlet and K. L. Virga, "Indoor propagation characteristics for wireless communications in the 30 GHz range," in IEEE Antennas and Propagation Society International Symposium (IEEE Cat. No.02CH37313), 2002.
- [35] M. Wang, Y. Liu, S. Li, Z. Chen, 60 GHz millimeter-wave propagation characteristics in indoor environment, in 2017 IEEE 9th International Conference on Communication Software and Networks (ICCSN), 2017.
- [36] G. Zhang, K. Saito, W. Fan, X. Cai, P. Hanpinitsak, J. Takada, G.F. Pedersen, Experimental characterization of millimeter-wave indoor propagation channels at 28 GHz, IEEE Access 6 (2018) 76516–76526.
- [37] M. Cheffena, Industrial indoor multipath propagation — A physical-statistical approach, in 2014 IEEE 25th Annual International Symposium on Personal, Indoor, and Mobile Radio Communication (PIMRC), 2014.
- [38] D. Ferreira, R.F.S. Caldeirinha, T.R. Fernandes, I. Cuiñas, Hollow clay brick wall propagation analysis and modified brick design for enhanced Wi-Fi coverage, IEEE Transactions on Antennas and Propagation 66 (2018) 331–339.
- [39] Y.L.C.D. Jong, J.A. Pugh, M. Bennai, P. Bouchard, 2.4 to 61 GHz multiband double-directional propagation measurements in indoor office environments, IEEE Transactions on Antennas and Propagation 66 (2018) 4806–4820.
- [40] I.D.S. Batalha, A.V.R. Lopes, J.P.L. Araújo, B.L.S. Castro, F.J. B. Barros, G.P.D.S. Cavalcante, E.G. Pelaes, Indoor corridor and office propagation measurements and channel models at 8, 9, 10 and 11 GHz, IEEE Access 7 (2019) 55005–55021.
- [41] J.W. Wallace, W. Ahmad, Y. Yang, R. Mehmood, M.A. Jensen, A comparison of indoor MIMO measurements and ray-tracing at 24 and 2.55 GHz, IEEE Transactions on Antennas and Propagation 65 (12) (2017) 6656–6668.
- [42] F. Mani, C. Oestges, A ray based indoor propagation model including depolarizing penetration, in 2009 3rd European Conference on Antennas and Propagation, 2009.
- [43] M.E. Diago-Mosquera, A. Aragón-Zavala, G. Castañón, Bringing it indoors: a review of narrowband radio propagation modeling for enclosed spaces, IEEE Access 8 (2020) 103875–103899.
- [44] Y.-K. Yoon, M.-W. Jung, J. Kim, Intelligent ray tracing for the propagation prediction, in Proceedings of the 2012 IEEE International Symposium on Antennas and Propagation, 2012.
- [45] C. Zhou, R. Jacksha, Modeling and measurement of radio propagation in tunnel environments, IEEE Antennas and Wireless Propagation Letters 16 (2017) 1431–1434.
- [46] L. Azpilicueta, M. Rawat, K. Rawat, F. Ghannouchi, F. Falcone, Convergence analysis in deterministic 3D ray launching radio channel estimation in complex environments, Applied Computational Electromagnetics Society Journal 29 (2014).
- [47] G. De la Roche, A. Alayón-Glazunov, B. Allen, LTE-advanced and next generation wireless networks: channel modelling and propagation, John Wiley & Sons, 2012.
- [48] M. Maria, S. Horna, L. Aveneau, Constrained convex space partition for ray tracing in architectural environments, in Computer Graphics Forum, 2017.
- [49] E.E. Tsiropoulou, G. Mitsis, S. Papavassiliou, Interest-aware energy collection & resource management in machine to machine communications, Ad Hoc Networks 68 (2018) 48–57.
- [50] S. Hussain, C. Brennan, Efficient preprocessed ray tracing for 5G mobile transmitter scenarios in urban microcellular environments, IEEE Transactions on Antennas and Propagation 67 (2019) 3323–3333.
- [51] X.C. Bo, X. Jin, J.F. Zhang, C.T. Jun, Study of corner singularity in conformal structured mesh generation for the finite-difference time-domain method based on ray tracing, IEEE Transactions on Microwave Theory and Techniques 67 (2019) 57–69.
- [52] N. Jeon, C. Lee, N. Kang, S. Kim, Performance of channel prediction using 3D ray-tracing scheme compared to conventional 2D scheme, in 2006 Asia-Pacific Conference on Communications, 2006.
- [53] X. Wu, Y. Zhang, C.-X. Wang, G. Goussetis, M. M. Alwakeel and others, "28 GHz indoor channel measurements and modelling in laboratory environment using directional antennas," in 2015 9th European Conference on Antennas and Propagation (EuCAP), 2015.
- [54] M. Lei, J. Zhang, T. Lei, D. Du, 28-GHz indoor channel measurements and analysis of propagation characteristics, in 2014 IEEE 25th Annual International Symposium on Personal, Indoor, and Mobile Radio Communication (PIMRC), 2014.
- [55] S. Deng, M.K. Samimi, T.S. Rappaport, 28 GHz and 73 GHz millimeter-wave indoor propagation measurements and path loss models, in 2015 IEEE International Conference on Communication Workshop (ICCW), 2015.
- [56] G.R. Maccartney, T.S. Rappaport, S. Sun, S. Deng, Indoor office wideband millimeter-wave propagation measurements and channel models at 28 and 73 GHz for ultra-dense 5G wireless networks, IEEE access 3 (2015) 2388–2424.
- [57] F. Hossain, T.K. Geok, T.A. Rahman, M.N. Hindia, K. Dimiyati, C.P. Tso, M.N. Kamaruddin, A smart 3D RT method: indoor radio wave propagation modelling at 28 GHz, Symmetry 11 (2019) 510.
- [58] F. Hossain, T. Kim Geok, T. Abd Rahman, M. Nour Hindia, K. Dimiyati, S. Ahmed, C.P. Tso, A. Abdaziz, W. Lim, A. Mahmud, T.C. Peng, Indoor 3-D RT radio wave propagation prediction method: PL and RSSI modeling validation by measurement at 4.5 GHz, Electronics 8 (7) (2019) 750.
- [59] T.K. Geok, F. Hossain, A.T.W. Chiat, A novel 3D ray launching technique for radio propagation prediction in indoor environments, PLoS One 13 (2018) e0201905.
- [60] T.K. Geok, F. Hossain, M.N. Kamaruddin, N.Z.A. Rahman, S. Thiagarajah, A.T.W. Chiat, C.P. Liew, A comprehensive review of efficient ray-tracing techniques for wireless communication, International Journal on Communications Antenna and Propagation 8 (2018) 123–136.
- [61] F. Hossain, T. Geok, S. Ahmed, Mohammadnourhinda, Minaasaduzzaman, A. Ahmad and M. Bari, "An adaptive 3-D ray tracing method for indoor radio wave propagation prediction," vol. 7, pp. 54-62, 2 2020.
- [62] K. Zhao, C. Gustafson, Q. Liao, S. Zhang, T. Bolin, Z. Ying, S. He, Channel characteristics and user body effects in an outdoor urban scenario at 15 and 28 GHz, IEEE Transactions on Antennas and Propagation 65 (2017) 6534–6548.
- [63] N. Blaunstein, C.G. Christodoulou, Antenna Fundamentals, in: in Radio propagation and adaptive antennas for wireless communication networks, 2014, pp. 34–53.
- [64] A. Kameni, B. Seny, L. Pichon, Multirate technique for explicit discontinuous galerkin computations of time-domain maxwell equations on complex geometries, IEEE Transactions on Magnetics 52 (2016) 1–4.
- [65] R. J. Adams and B. A. Davis, "Fresnel integral equations," in IEEE Antennas and Propagation Society International Symposium. Digest. Held in conjunction with: USNC/CNC/URSI North American Radio Sci. Meeting (Cat. No.03CH37450), 2003.

- [66] K. Uchida, L. Barolli, Dijkstra-algorithm based ray-tracing by controlling proximity node mapping, in 2017 31st International Conference on Advanced Information Networking and Applications Workshops (WAINA), 2017.
- [67] H.M. El-Sallabi, G. Liang, H.L. Bertoni, I.T. Rekanos, P. Vainikainen, Influence of diffraction coefficient and corner shape on ray prediction of power and delay spread in urban microcells, *IEEE Transactions on Antennas and Propagation* 50 (2002) 703–712.
- [68] S. Helhel, Comparison of 900 and 1800 MHz indoor propagation deterioration, *IEEE transactions on antennas and propagation* 54 (2006) 3921–3924.

Further reading

- [69] M.B. Majed, T.A. Rahman, O.A. Aziz, M.N. Hindia, E. Hanafi, Channel characterization and path loss modeling in indoor environment at 4.5, 28, and 38 GHz for 5G cellular networks, *International Journal of Antennas and Propagation* 2018 (2018).
- [70] Q. Hong, J. Zhang, H. Zheng, H. Li, H. Hu, B. Zhang, Z. Lai, J. Zhang, The impact of antenna height on 3D channel: a ray launching based analysis, *Electronics* 7 (2018) 2.
- [71] V. Monebhurrn, Numerical and experimental investigations of base station antenna height on cellular network coverage, *IEEE Transactions on Antennas and Propagation* 66 (2018) 6563–6569.
- [72] A. Ando, T. Ito, H. Yoshioka, H. Tsuboi, H. Nakamura, Effects of receiver antenna height and polarization on received signal levels at road level from transmitter antennas set in manhole, in 2011 IEEE International Symposium on Antennas and Propagation (APSURSI), 2011.
- [73] P. Series, “Effects of building materials and structures on radiowave propagation above about 100 MHz,” Recommendation ITU-R, p. 2040–1, 2015.
- [74] J.-H. Lee, J.-S. Choi, J.-Y. Lee, S.-C. Kim, Permittivity effect of building materials on 28 GHz mmWave channel using 3D ray tracing simulation, in *GLOBECOM 2017–2017 IEEE Global Communications Conference*, 2017.
- [75] F.L. Granda, L. Azpilicueta, D. Aguilar, C. Vargas, 3D ray launching simulation of urban vehicle to infrastructure radio propagation links, in *Congreso de Ciencia y Tecnología ESPE*, 2018.
- [76] S. Sun, G.R. MacCartney, T.S. Rappaport, Millimeter-wave distance-dependent large-scale propagation measurements and path loss models for outdoor and indoor 5G systems, in 2016 10th European Conference on Antennas and Propagation (EuCAP), 2016.
- [77] F. Hossain, T.K. Geok, T.A. Rahman, M.N. Hindia, K. Dimiyati, S. Ahmed, C.P. Tso, N.Z. Abd Rahman, An efficient 3-D ray tracing method: prediction of indoor radio propagation at 28 GHz in 5G network, *Electronics* 8 (2019) 286.
- [78] F. Hossain, T.K. Geok, T.A. Rahman, M.N. Hindia, K. Dimiyati, A. Abdaziz, Indoor millimeter-wave propagation prediction by measurement and ray tracing simulation at 38 GHz, *Symmetry* 10 (2018) 464.
- [79] M.A. Fares, S.C. Fares, C.A. Ventrice, Comparison between the phase shifts of the electromagnetic waves due to moist snow and wet snow, in *Proceedings of the IEEE SoutheastCon 2006*, 2006.
- [80] Y.S. Meng, Y.H. Lee, B.C. Ng, Investigation of rainfall effect on forested radio wave propagation, *IEEE Antennas and Wireless Propagation Letters* 7 (2008) 159–162.
- [81] L. Luini, A. Quadri, Investigation and modeling of ice clouds affecting Earth-space communication systems, *IEEE Transactions on Antennas and Propagation* 66 (2018) 360–367.

- [82] M. Biscarini, L. Milani, M. Montopoli, K.D. Sanctis, S.D. Fabio, K.M. Magde, G.A. Brost, F.S. Marzano, Exploiting tropospheric measurements from Sun-tracking radiometer for radiopropagation models at centimeter and millimeter wave, *IEEE Journal of Selected Topics in Applied Earth Observations and Remote Sensing* 12 (2019) 1697–1708.
- [83] C. Briso, C. Calvo, Y. Xu, UWB propagation measurements and modelling in large indoor environments, *IEEE Access* 7 (2019) 41913–41920.

Tan KIM GEOK received the B.E., M.E., and PhD. degrees from the University of Technology Malaysia, in 1995, 1997, and 2000, respectively, all in electrical engineering. He has been a Senior R&D Engineer with EPCOS, Singapore, in 2000. From 2001 to 2003, he joined DoCoMo Euro-Labs, Munich, Germany. He is currently an Academic Staff with Multimedia University. His research interests include radio propagation for outdoor and indoor, RFID, multiuser detection technique for multicarrier technologies, and A-GPS.

FERDOUS HOSSAIN received the B.Sc. degree in computer science and engineering and the M.Sc. degree in information and communication technology from Mawlana Bhashani Science and Technology University, Bangladesh, in 2012 and 2015, respectively, and the PhD degree in engineering from the Faculty of Engineering and Technology, Multimedia University, Malaysia, in 2019. He was a recipient of the Best PhD thesis award for the Doctor of Philosophy (Engineering) Award in 2020. He has authored and co-authored several international journals and conference papers. His research areas include radio propagation for outdoor and indoor, image processing, and big data analysis.

SHARUL KAMAL ABDUL RAHIM received the degree in electrical engineering from The University of Tennessee, USA, the M.Sc. degree in engineering (communication engineering) from Universiti Teknologi Malaysia (UTM), and the Ph.D. degree in wireless communication system from the University of Birmingham, U.K., in 2007. After his graduation from The University of Tennessee, he spent three years in industry. After graduating the M.Sc. degree, he joined UTM in 2001, where he is currently a Professor with the Wireless Communication Center. He has published over 200 learned articles, including the *IEEE Antenna and Propagation Magazine*, the *IEEE Transactions on Antenna and Propagation*, *IEEE Antenna and Propagation Letters*, and obtained various patents. His research interests include antenna design, smart antenna systems, beamforming networks, and microwave devices for fifth generation mobile communication. He is also a Senior Member of IEEE Malaysia Section, a member of The Institute of Engineers, Malaysia, a Professional Engineer with BEM, and a member of the Eta Kappa Nu Chapter, The University of Tennessee, and the International Electrical Engineering Honor Society. He is also an Executive Committee of the IEM Southern Branch.

OLAKUNLE ELIJAH received the B.Eng. degree from the Federal University of Technology Minna, Minna, Nigeria, in 2003, the M.Sc. degree in micro-electronics and computing from Bournemouth University, Poole, U.K., in 2008, the postgraduate degree in advance microelectronics from Bolton University, Bolton, U.K., in 2010, and the Ph.D. degree from Universiti Teknologi Malaysia, Johor Bahru, Malaysia, in 2018. He was a Field Engineer with Kuyet Nigeria Ltd., Lagos, Nigeria, in 2006. From 2011 to 2013, he was the MD/CEO with Mircoscale Embedded Ltd., Abuja, Nigeria. He is currently conducting research in the field of wireless communications and the IoT as a Postdoctoral Fellow with the Wireless Communication Centre, Higher Institution Centre of Excellence (HiCoE), Malaysia. His current research interests include embedded systems, wireless communication, massive MIMO, interference mitigation, heterogeneous networks, the IoT with data analysis, and 5G and beyond.

AKAA AGBAEZE ETENG obtained a B.Eng degree in Electrical/Electronic Engineering from the Federal University of Technology Owerri, Nigeria in 2002, and a M. Eng. degree in Telecommunications and Electronics from the University of Port Harcourt, Nigeria in 2008. In 2016, he obtained a Ph.D. in Electrical Engineering from Universiti Teknologi Malaysia. He is currently a lecturer at the Department of Electrical/Electronic Engineering at the University of Port Harcourt, Nigeria. His research interests include wireless energy transfer, radio frequency energy harvesting, and wireless powered communications.

CHUN THENG LOH is currently pursuing the bachelor's degree in Electronics engineering majoring in telecommunications in Faculty of Engineering and Technology (FET), Multimedia University (MMU) Melaka, Malaysia. He is in his final year of degree and expected to graduate in March 2021. His research interests include radio propagation, internet-of-things and circuit designs.

LIM LILI received her Advanced Diploma in Technology (Electronics Engineering) from Tunku Abdul Rahman College (TARC) and subsequently obtained a M.Sc. in Electronics from Queen's University of Belfast. In 2019, she obtained her PhD in Electrical and Electronics Engineering from University of Nottingham Malaysia in the area of MIMO channel coding and equalisation. Her current research interest is in statistical signal and image processing, machine learning, and next generation wireless communication signal processing.

C. P. TSO, a Malaysian engineering educator, and researcher, received his Bachelor's degree from Loughborough in 1968, through a National Electricity Board scholarship, Master's from Massachusetts Institute of Technology through research assistantship, and Ph.D. from University of California, Berkeley, in 1979, through a Fulbright-Hays scholarship.

He has worked at the University of Malaya, Nanyang Technological University, and Multimedia University.

THAREK ABD RAHMAN received the B.Sc. degree in electrical and electronic engineering from the University of Strathclyde, U.K., in 1979, the M.Sc. degree in communication engineering from UMIST, Manchester, U.K., and the Ph.D. degree in mobile radio communication engineering from the University of Bristol, U.K., in 1988. He is currently the Director of the Wireless Communication Centre, Universiti Teknologi Malaysia, and also a Professor with the Faculty of Electrical Engineering. He has also conducted various short courses related to mobile and satellite communication to the Telecommunication Industry and Government body, since 1990. He has teaching experience in the areas of mobile radio, wireless communication system, and satellite communication. He has published more than 120 papers related to wireless communication in national/international journal and conference. His research interests include radio propagation, antenna and RF design, and indoors and outdoors wireless communication.

M. NOUR HINDIA received the Ph.D. degree from the Faculty of Engineering in Telecommunication, University of Malaya, in 2015. He is working in the field of wireless communications, especially in channel sounding, network planning, converge estimation, handover, scheduling, and quality-of-service enhancement for 5G Networks. He is also working with Research Group in Modulation and Coding Scheme for the Internet of Thing for Future Networks. He has authored or co-authored a number of Science Citation Index (SCI) journals and conference papers. He has also participated as a Reviewer and a Committee Member of a number of ISI journals and conferences.